Master's thesis

NTNU
Norwegian University of Science and Technology
Faculty of Engineering
Department of Geoscience and Petroleum

Kamilla Berg Dalseth

Quantifying the effects of feeder chimneys on trapping mechanisms at the Sleipner CO2 storage site

Master's thesis in Master of Science in Petroleum Geoscience and Engineering

Supervisor: Philip Ringrose

August 2020

NTNU
Norwegian University of Science and Technology

Kamilla Berg Dalseth

Quantifying the effects of feeder chimneys on trapping mechanisms at the Sleipner CO2 storage site

Master's thesis in Master of Science in Petroleum Geoscience and Engineering
Supervisor: Philip Ringrose
August 2020

Norwegian University of Science and Technology
Faculty of Engineering
Department of Geoscience and Petroleum

NTNU
Kunnskap for en bedre verden

Summary

CO_2 injection at Sleipner into the shallow marine sand of Utsira Fm began in 1996, and is still ongoing. The plume has been monitored with nine time lapse seismic reflection surveys. From the repeated seismic surveys nine strong seismic reflections has been quantified as a result of CO_2 replacing brine, and further been interpreted as CO_2 distributed beneath nine layers of thin shale within the otherwise homogeneous reservoir.

However, vertical features of disturbed or dimmed amplitudes interpreted as feeder chimneys are also observed. Additionally, several CO_2 plume layers develop separately from the other layers, without any associated feeder chimneys. From these observations, feeder chimneys have been interpreted indirectly as an explanation for the lateral and vertical migration. The main goal of this work is to improve the geological interpretation of these features from flow modelling using Eclipse 300.

The project will use the newly published Sleipner data from the CO_2 storage data consortium. The datasets available include; Seismic data, injection well datasets and flow modelling datasets. The project will use the Sleipner 2019 Benchmark Model, supported by the 4D seismic data up to 2010. Quantifying the effects of the vertical feeders will be the main focus along with geological interpretation and analysis of the dynamic flow effects of the vertical feeders at the Sleipner CO_2 storage site. This will improve understanding of CO_2 migration, both vertically and laterally, and leakage detection.

Sammendrag

CO_2 lagring fra Sleipner Øst feltet i akviferen Utsira Fm har foregått siden 1996. CO_2-akkumulasjonen overvåkes nøye for å forhindre lekkasje, dette har blant annet foregått ved flere gjentatte seismiske undersøkelser. Fra disse gjentatte seismiske undersøkelsene har ni sterke seismiske refleksjoner blitt kvantifiser som CO_2 som erstatter vannet i akviferen, og videre tolket som CO_2 distribuert under ni lag med tynn skifer inni det ellers homogene reservoaret.

Videre, er det blitt observert vertikale soner av forstyrrende eller nedtonede amplituder tolket som *feeder chimneys*. I tillegg utvikler flere av CO_2 lagene seg uavhengig fra de andre lagene, og uten tilknytning observerte *feeder chimneys*. Fra disse observasjonene er *feeder chimneys* indirekte tolket som en forklaring på den laterale og vertikale migrasjonen.

Hovedmålet med dette arbeidet er å forbedre den geologiske forståelsen av disse *feeder chimneys*, og de resulterende dynamiske strømningseffektene.

Dette prosjektet vil bruke de nylig publiserte Sleipner-dataene fra *the CO2 storage data consortium*. Datasettene inkluderer: flowmodelling dataset, seismiske data og brønndata. Prosjektet vil bruke *Sleipner 2019 Benchmark Model*, støttet av 4D seismiske data fra 1994 frem til 2010.

Kvantifisere effektene av de vertikale *feeder chimneys* vil være hovedfokuset. Dette vil bli gjort gjennom en Eclipse 300 modellering av CO_2 akkumulasjonen, hvor egenskapene endres til å likne ulike typer geologi. Målet er å forbedre den geologiske forståelsen og forståelsen for CO_2-migrasjon, både vertikalt og horisontalt, samt lekkasjedeteksjon.

Acknowledgement

This study is the result of my Master Thesis completing my Master's degree in Petroleum Geoscience and Engineering at NTNU. The project started in Feburary, and was written during the spring and summer of 2020.

I would like to thank my advisor Philip Ringrose for presenting the idea of the Thesis to me, and for guidance through the project. I also want to thank Adeel Zahid at Equinor for providing an Eclipse E300 model, and answers to questions throughout the process. Furthermore, I want to thank Per Arne Slotte at NTNU for help with Eclipse.

This Thesis would not be possible without several datasets being made available. I want to thank the SINTEF-led CO2 Data Share Consortium for publishing open access data, and Equinor for releasing the Sleipner datasets.

March 12th 2020 a national lockdown was announced as a response to the ongoing COVID-19 - pandemic. This included all educational institutions closed, including NTNU. Thus, this report is mainly developed at home during social distancing. With this in mind, I want to thank Lars Johan Sandvik at NTNU for help to set up Remote Desktop, and making it possible to work from home.

Moreover, I want to thank my colleagues at Equinor Virtual Summer Internship for moral support and help to keep my spirits high over the summer.

Finally, I want to thank my family for always being supportive, and a source of inspiration.

Kamilla Berg Dalseth
Oslo, August 7th, 2020

Table of Contents

List of Tables

List of Figures

Abbreviations

CCS	=	Carbon Capture and Storage
CO_2	=	Carbon Dioxide
IFT	=	Interfacial Tension
IOR	=	Improved Oil Recovery
MFC	=	Main Feeder Chimney

Chapter 1

Introduction

1.1 Area of interest

The Sleipner gas field is located in the North Sea, 250km from the Norwegian coastline, Figure 1.1 A. CO_2 has been injected in the Utsira Fm through injection well 15/9-A-16 since September 15th 1996 (Furre et al., 2017), and by the end of 2018 nearly 18Mt CO_2 had been injected. Injection has continued uninterrupted since the beginning, apart from regular maintenance of the platform (Furre et al., 2019).

1.2 Background

The background for the Sleipner CO_2 disposal project was the challenge of high CO_2 content in the gas from Sleipner Vest gas field. The Sleipner reservoir is faulted, with different pressure regimes and different fluid properties, where the CO_2 content varies between 4 - 9.5%. The gas from Sleipner were to be sold under the he Troll Gas Sales Agreement. To meet the sales gas requirements of maximum 2.5% by volume CO_2 in the sales gas delivered to the pipeline CO_2 needed to be separated from the produced gas. This requirement combined with increased environmental concern in the early planning of the field development raised the question of alternatives to atmospheric release of the removed CO_2. Various alternatives for disposal of the CO_2 from the Sleipner fields were investigated in the early 1990's.

One alternative was to export the CO_2 into an oil field for IOR purpose, but analysis of injection rates showed this would only partly solve the problem. A second proposal was to inject the removed CO_2 into the producing gas/condensate reservoir at the Sleipner Øst Field, Heimdal Fm, for improved condensate recovery. Recycling of gas to increase condensate recovery was already planned, and the risk of CO_2 replacing hydrocarbon gas in the recycling was a possibility. A third solution was to dispose of the CO_2 and inject it into the aquifer of Heimdal Fm, but then risking contaminating the gas production from the reservoir.

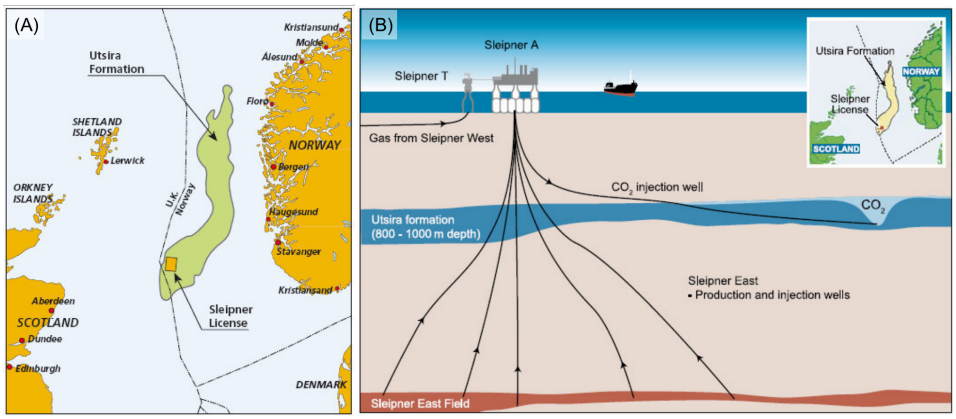

Figure 1.1: (A) Location of the Sleipner Area in yellow square, and extent of the Utsira Fm in green. (B) Simplified overview of the Sleipner Øst gas field. The gas reservoir with production wells, and CO_2 injection well into the Utsira Fm. Figures modified from Solomon (2007)

This left the option to inject the CO_2 into a separate aquifer. Here, two formations were evaluated as reservoir options for the project, the Utsira Fm at 800m depth, Figure 1.1 B, and Skagerak Fm at 2500m depth. The Utsira was chosen due to better reservoir quality, shallower depth and lower well and top side costs. The disadvantages of Utsira Fm could be unconsolidated rock and sub-critical conditions for the CO_2. Neither was considered to be of major concern (Baklid et al., 1996). Some challenges related to injectivity were encountered during the first year related to sand influx, but were resolved after re-perforation and instillation of a gravel pack in August 1997. Since then injection has been stable, with an injection rate of approximately 0.9Mt during the first years. Reduced gas flow from Sleipner resulted in some reduction during later years, but since 2014 CO_2 from the Gudrun gas field has also been processed via the Sleipner CCS facility (Furre et al., 2017).

1.3 Problem Definition and Approach

The main goal of this work is to improve the geological interpretation of feeder chimneys observed in the seismic data, and to improve the understanding of the resulting flow effects. This is important to better understand how CO_2 behave in the reservoir, and thus improve conformance monitoring. To achieve this, a literature review is preformed to get an understanding of the Sleipner storage site and previous work. Further, the newly published Sleipner data from the CO_2 Storage Data Consortium, this include the seismic data, injection well datasets and flow modelling datasets, will be used. Simulations in Eclipse 300 will be preformed to model the flow effects of the geological interpretations of the vertical feeders and migration. Finally, a qualitative comparison to the seismic data will be preformed to identify what modelling scenario is the best fit. To decide best fit, the elements investigated will be:

- Arrival of CO_2 at the top reservoir.
- Top layer geometry.
- Plume layering.

1.4 Limitations

The main limitation for this project is time, this thesis has been developed over a semester. Furthermore, the initial plan was to also include capillary pressure and threshold pressure curves for the shales. However, this was disregarded due to the on going COVID-19 pandemic and that this thesis has mainly been developed at home. The home office also brought with it some challenges, as Petrel would not run due to too low screen resolution. As a consequence, the seismic interpretation is more limited than initially planned.

Structure of Report

Chapter 2 covers the geological and tectonic setting of the Utsira Fm, and characterization of reservoir and caprock properties from literature. Moreover, previous work is summarized.
Chapter 3 presents a theoretical background of CO_2, Carbon Capture and Storage (CCS) and monitoring techniques used to verify containment.
Chapter 4 describe the data and modelling scheme.
Chapter 5 present main results and discussion.
Lastly, **Chapter 6** cover Conclusions and Recommendations for Future Work.

Chapter 2

Literature Review

2.1 Geological and Tectonic Setting

The structural framework of the North Sea is a result of Upper Jurassic and Lower Cretaceous rifting, and movement of the Upper Permian Zechstein salt. The halokinesis generated by bouyancy forces is important for generation of closed structures, including hydrocarbon traps, and in the southern North Sea also control local topography and further sedimentation (Halland et al., 2019).

In Paleogene and Neogene the North Sea was stable, but still experienced thermal subsidence. The biggest subsidence was experienced over the rift structures from Upper Jurassic, Viking Graben and Central Graben, due to more heating of the rift axis and thus greater cooling and thermal subsidence along these structures.

The storage reservoir is the late Miocene Utsira Fm and the Pliocene Sand Wedge, Figure 2.1. Nicoll (2011) describe the underlying mid-Miocene Hordaland Group Shales to be characterized by polygonal faulting, soft sediment deformation and mud diapirism. Mud diapirs up to 100 meters high and $\sim$ 1-2km in diameter are onlapped by the Utsira Fm, creating thickness variations on a local scale. The Utsira Fm and Hordaland/Nordland interface is generally regarded as an regional unconformity, due to evidence of erosion prior to deposition of the Utsira Fm.

The overlying Pleistocene to Holocene sequence of the Nordland Group Mudstones ($\sim$ 2.5-0 Ma) represents a deep water, transitional environment. These units have been sub divided into three units; the Shale Drape, the Prograding Unit and the remaining Pleistocene to Holocene unit.

During the Neogene thick sequences was deposited in the North Sea from uplift glacial erosion of the Norwegian mainland (Halland et al., 2019). Erosional unconformities indicates that the ice was in contact with the seabed at multiple occasions. The latest ice sheet (Late Devensian) has left well-preserved sediments to record its position and demise. Reconstructions indicate that the ice had a thickness of 1000m and was grounded over the Sleipner area of the Northern North Sea (Cavanagh and Haszeldine, 2014).

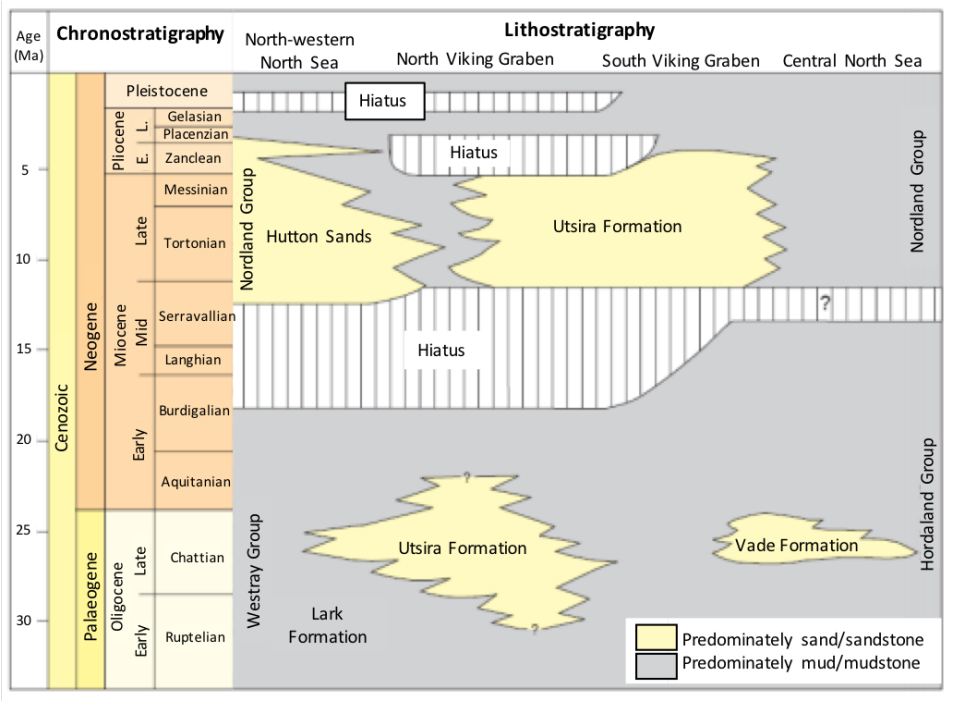

Figure 2.1: Stratigraphic correlation chart for Hordaland and Nordland Groups. Edited from Fyfe et al. (2003)

2.1.1 Utsira Fm and the Sand Wedge, Reservoir Characterization and Geology

The storage reservoir compromises the Miocene Utsira Formation and the overlaying Pliocene Sand Wedge. It consist of mainly unconsolidated sand with a number of thin mudstone layers (White et al., 2018).

From the Completion Report from Well 15/9-13 the lithological description reads: "The Utsira Fm consist of sand with some stringers of clay. The sand is composed of clear, very fine to medium quartz grains, which are sub-angular to sub-rounded. The clay is light grey to grey, soft, sticky and calcareous. Traces of mica, pyrite, glauconite, shell fragments and foraminifers are recognized." And the depositional environment is established to be marine, inner to outer shelf, with the Utsira Fm indicating inner shelf.

Chadwick et al. (2004b) describe the Utsira Fm to be a basinally restricted, fine grained, unconsolidated sandstone deposit. Extending more than 400 km from North to South, and between 50 to 100 km from East to West. In the west and east the limits are defined by stratigraphical onlap, to the south-west passing laterally into finer grained sediments, and to the north occupying a deepning, narrow channel.

Halland et al. (2019) describe how the Utsira Fm display a complex architecture, and are marine sandstones with source area to the west. This coincides with the interpretation of Ramberg et al. (2013), with deposition in a shallow marine environment. A deltaic system developed on the Shetland Platform approximately 12 million years ago, the delta plain located in what today is the UK sector of the North Sea, the coastal line approximately located at the Norwegian-English border, and in the Norwegian part of the North Sea huge amount of fine grained sand was deposited and reworked by ocean currents.

Chadwick et al. (2004b) have described the Utsira Sand have internal structures of stacked overlapping sand 'mounds' of low relief, and interpret these structures as fan lobes and serrated by thin intra-reservoir mudstone or shaly horizons. Further, interpreting this as a composite low-stand fan, deposited by mass flows in marine environment with water depths of 100m or more.

Further, Chadwick et al. (2004b) also identify two main depocenters of the Utsira sand from isopach map of the reservoir, one depocenter located in the South, around Sleipner, thickness locally exceeding 300m and a second depocenter to the North with thickness approaching 200m. Locally depositional patterns are quite complex with isolated depocenters, and lesser areas of non-deposition within the main depocentre.

The mudstone layers are below the resolution of the seismic data, and cannot be correlated between local wells (White et al., 2018).

The uppermost sand separated from the Utsira Fm by a 5m shale, the Pliocene sand, often referred to as the Sand Wedge was previously assigned to the Utsira Fm (Halland et al., 2019). The interpretation of this unit is the re-establishment of sand-dominated deposition system (Fyfe et al., 2003).

2.1.2 Nordland Group Caprock Geology

The caprock of the injection site, the Nordland Group, consist of predominantly shale, and are divided into three units; the lowest Shale Drape, middle Pliocene prograding units, and uppermost Quarternary glacio-marine clays and glacial tills. The Shale Drape, or

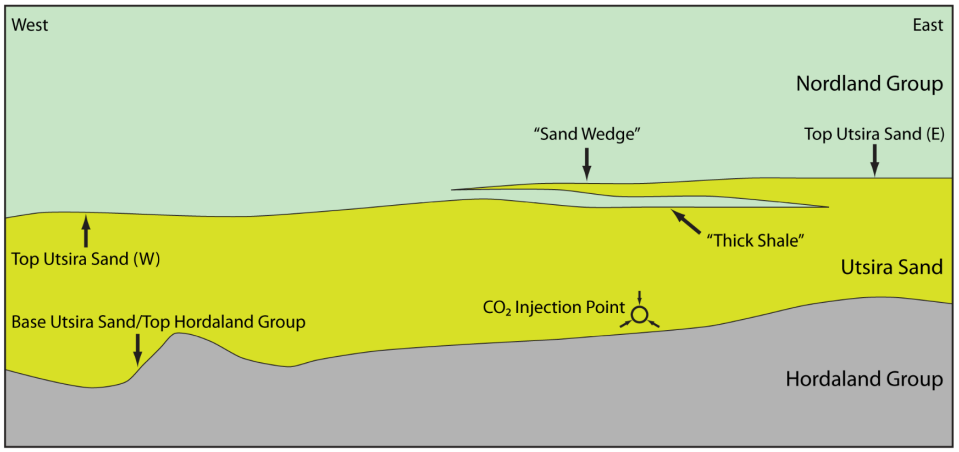

Figure 2.2: West-East cross section of the Utsira and the Sand Wedge, not to scale. Illustration without intra-reservoir shales in the Utsira Fm. Figure from Nicoll (2011).

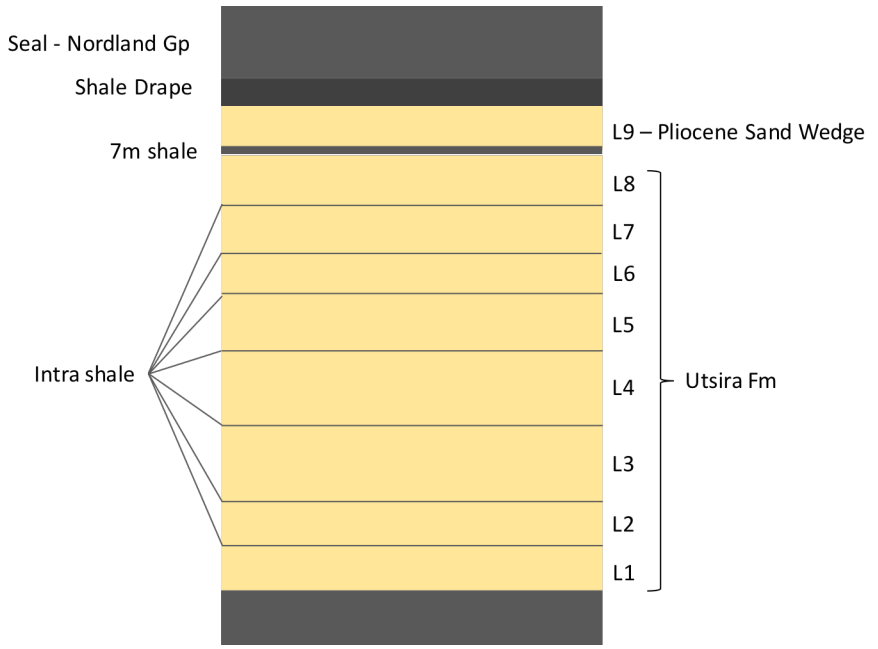

Figure 2.3: Simple overview of the storage reservoir architecture. Made with Microsoft Power Point

Lower Seal, is described as a shaly unit with a thickness of 50-150 meters, overlying the Utsira Fm. It is considered to be a basal surface for downlapping clinoforms from an overlying prograding sequence. In the Sleipner area the Shale Drape is 50 meters, but thins to 25 meters where the Sand Wedge is present. The Prograding Unit, Middle Seal, is characterized by series of clinoforms prograding from the East to the West into the basin centre. Within the basin centre shaly sediments dominate, but the sediments coarsen upwards and laterally into sandier facies towards the basin margins. The upper unit, forms a basal regional unconformity, truncating the surface of the underlying Prograding Unit. This unit is predominately compromised of glacial tills and glacio-marine clays (Nicoll, 2011).

2.2 Monitoring at Sleipner

A summary of the monitoring at Sleipner in table 2.1. In 1994, before injection start in 1996, a baseline 3D seismic survey was performed. After this multiple monitoring surveys have been recorded, in 1999, 2001, 2004, 2006, 2008, 2010 and 2013 respectively (Furre et al., 2017). The seismic monitoring program aims are twofold; first and foremost it is to track storage performance and assure storage integrity. Second, via a number of scientific research projects, to test and refine monitoring tools and to improve understanding of CO_2 migration and trapping mechanisms in the storage reservoir (Chadwick and Eiken, 2013).

Gravity measurements are also used to monitor the plume. Permanent seabed benchmarks were installed in 2002, and a baseline for gravity monitoring was acquired the same year. Subsequent surveys were conducted in 2005, 2009 and 2013. New benchmarks stations have been installed, covering a larger area, as the plume has expanded over time.

In 2008 a Controlled Source Electromagnetic (CSEM) test line was acquired over the field. The survey had conventional configuration, i.e. surface-to-surface. 27 seabed receivers were deployed, covering about 9.5km. 6 groups of in total 9 seabed pipes crossed the CSEM survey line which created a challenge interpreting the data as it interfered with the CSEM data (Parka et al., 2013). At the time the CO_2 plume was challenging to detect on the CSEM, the resolution was too poor, and consequently not repeated (Furre et al., 2017).

Additionally, chemical sampling of the sediments and water column has been conducted, in search of potential increased CO_2 levels. None of the monitoring techniques have indicated any leakage from the Sleipner CO_2 injection site (Furre et al., 2017).

2.3 Previous Work

Prior to injection the baseline seismic survey provided an interpretation of the topography of the reservoir unit, the Utsira Sand. Establishing that the top structure was relatively flat, but with some domal and anticlinal structures linked by saddles. The injection site is located below a dome of approx. 1600m and a height of approx. 12m abouve its spill point (Lindeberg et al., 2000). Due to the structure of the Utsira is fairly flat, it was difficult to predict plume migration pre-injection. Thus, prior to injection a ”black oil”-type simulation of the CO_2 plume was preformed in Eclipse. Using a 3 phase gas-oil

What	Preformed
Wellhead monitoring	✓
Downhole fluid sampling	✓
4D seismic	1994 (baseline), 1999, 2001, 2002, 2004, 2006, 2008, 2010, 2013, 2016
4D gravity	2002 (baseline), 2005, 2009, 2013
Controlled Source Electromagnetic (CSEM)	2008
Seabed/marine surveys	✓
Surface/shallow gas	✓

Table 2.1: An overview of monitoring at the Sleipner storage site (Furre et al. (2017), Parka et al. (2013))

description, applying CO_2 properties to the gas-phase, water properties to the oil-phase. The goal of the 3 phase simulation was to try to simulate the solubility of the CO_2 in water. The result of the simulation predicted a cone plume, and a maximum extent of the plume in 3km in any direction after 20 years. The results from the study also predicted 18% of the CO_2 to be dissolved in the formation water (Baklid et al., 1996).

Analysis of the seismic and wireline-logs indicate that the reservoir sand is mostly homogeneous, but for the numerous thin inter-shale layers. Lindeberg et al. (2000) claims up to 14 thin shale layers, that follow the topography of the Top Utsira sand. In other words, they have a domal geometry above the injection site. Further, Lindeberg et al. (2000) imply that the shale layers are not fully impermeable based on assumptions about the depositional processes (partial erosion) and about post-depositional deformation (differential compaction).

Interpretations of the first seismic survey in 1999, a small amplitude change was observed in Layer 9, the Sand wedge. From the small change in amplitude, the interpretation was that the CO_2 had just reached that level. Thus, the injected CO_2 migrated from the injection point at 1012TVD to the top of the structure in under 3 years, ascending over 200m. The short migration time from the injection point to the top of the reservoir bring to question the sealing properties of the intra-shales (Cavanagh and Haszeldine, 2014).

Some unexplained aspects of the plume summarized by Cavanagh and Haszeldine (2014); first, the uncertainty concerning the mass balance of the plume. Second, the CO_2 columns trapped beneath the intra-shale layers are unexpectedly low despite uncertainties about the layer thicknesses. Estimates for the column height consistently fall within the range 7-14m. Third, the plume flow behaviour is not indicative of sealing shale barriers punctuated by faults, holes or penetrated by a high permeability chimney or sand injectite.

Cavanagh and Haszeldine (2014) preformed two modelling scenarios, both with identical geometry, but varying threshold pressures of the intra-shales of the Utsira Fm. First, a base case applying the threshold pressure measured from cores recovered from the Lower Seal, 1.6 - 1.9MPa, and assume this is representative for all intra-shale barriers within the model. The base case resulted in a 'zig-zag' pattern of predominately lateral migration, not matching the observed CO_2 distribution observed from seismic data. Moreover, the base case simulation failed to reach the caprock, as the CO_2 did not breach the 7m thick Lower Seal, but proceeded to backfilled the reservoir with a column height of several hundred

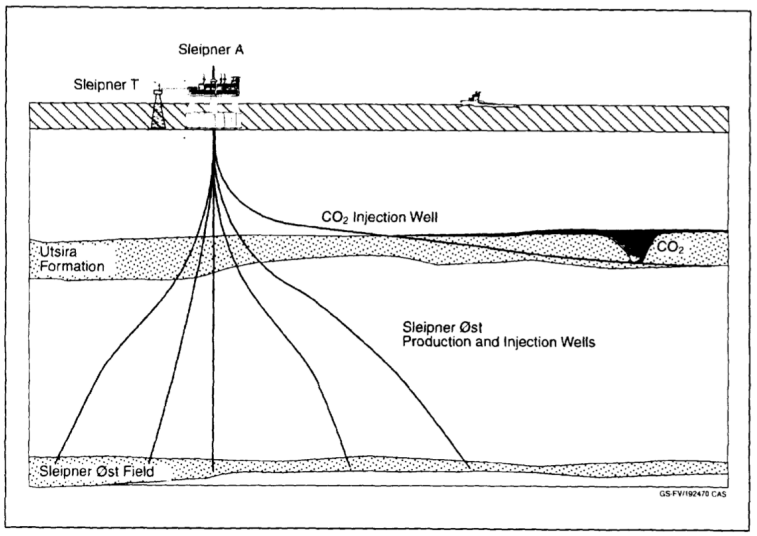

Figure 2.4: Pre-injection simulation of CO_2 plume distribution with injection well, to scale, from Baklid et al. (1996).

meters eventually saturating the entire reservoir. The second scenario, identical to the base case with the exception of the threshold pressure. The threshold pressure was gradually reduced with iterative experimentation until the model exhibited thin CO_2 layers similar to those observed. The second scenario matching the observed plume perfectly, exhibit surprisingly low threshold pressures, two orders of magnitude lower than the laboratory values measured on the caprock from well 15/9A-11. The breakthrough condition may be as low as 50kPa. Further, Cavanagh and Haszeldine (2014) infer that the explanation for the low breakthrough pressures can be traced back to micro-fractures spanning the shale barriers within Utsira Fm, and present ice sheet unloading as a possible mechanism of pre-injection fracturing.

Chadwick et al. (2004a) on the other hand, states that there is little evidence of pre-injection faulting in the 1994 data within the upper part of the reservoir. However, they do open for the possibility of small faults close to the limit of seismic resolution, as a result of differential compaction. Further, Chadwick et al. (2004a) discuss how CO_2 could dehydrate the shales and induce shrinkage cracks. Alternatively, Chadwick et al. (2004a) propose that the force of the CO_2 column is able to displace the thin shale layers in the weak, unconsolidated sediments by pure mechanical force.

The shale layers are not possible to correlate between wells (Furre et al., 2017). Not continuous shale layers, not acting as continuous barriers throughout, could explain the short migration time to the top. However, Cavanagh and Haszeldine (2014) argue that if the shale layers acted as seals, but are not continuous, preventing vertical migration the plume would have taken much longer time to breakthrough. Resulting, in a more 'zig-zag' distribution with lateral offsets as a result of CO_2 tracking along the base of each shale layer until finding a pathway to migrate vertically, before repeating this behaviour,

as observed in the base case modeling.

Ganesh et al. (2013) present simulations of CO_2 migration for various rocks, and explore the flow regime of bouyancy/capillary flow. With the assumption that bouyancy-dominated plume migration through time and distance falls into three regimes; compact flow, capillary flow and secondary accumulation beneath a seal. Concluding that in the capillary channel regime depends on the degree of heterogeneity, and varies between finger-like and back-filling. Fingering pattern is the least effective in terms of storage capacity, with minimal rock contact. Backfilled, 'compact', distributions of CO_2 saturations on the other hand, have much greater storage efficiency, and occur in more heterogeneous fabrics with a wider range of threshold pressure, as a result of poorer sorting or wider grain size distributions.

Further, White et al. (2018) highlight the importance of learning as much as possible about layer geometry in order to understand the controlling flow processes in the plume. No well-record are available from within the plume itself. This is where seismic data is key, and the outer limit of CO_2 reflectivity correspond to the CO_2-water contact (CWC). However, mapping individual layer thickness has proved challenging, and layer reflectivity is generally dominated by 'thin layer' tuning effects. White et al. (2018) focuses on determining temporal thickness of the topmost layer, which is clearly imaged and suffer no signal attenuation or dispersion from overlying layers. The temporal thickness, two-way travel-time thickness, do not correspond exactly to true (depth) layer thickness, however, temporal thickness can provide important constraints on layer geometry and spreading process. Since the CO_2 reached the top reservoir in 1999, the topmost layer has grown rapidly, being fed from below, and developed laterally beneath the topseal topography via a fill and spill process.

Furthermore, Furre et al. (2019) identify feeder chimneys, both observable as vertical features of disturbed or dimmed amplitudes and not observable, but implied from individual plume layer growing separately from others. The main feeder chimney (MFC), is identified as a vertical feature disturbed or dimmed amplitudes. *Chimney NE1* and *Chimney SW1* are implied. *Chimney NE1* is located 800m NE of the injection point, and indications of this invisible feeder chimney appeared already in the first time lapse survey in 1999, when Layer 6 was identified to be growing separate from the main feeder chimney and possibly sourced from the directly underlying northeastern part of Layer 5. At the same time northward lateral migration of Layer 5 appears to slow down. By further inspecting the area, Furre et al. (2019) indicate that Layer 4 grew offset from the MFC, indicating a potential feeder chimney existing from Layer 2 or potentially Layer 3 through layers 4 and 5 to Layer 6. In 1999 there are no indication of migration to Layers 7 and 8 at this location. However, in 2001 the northern part of Layer 9 had developed just above the *Chimney NE1* location. Thus, there are a possibility that Layer 9 is fed directly from Layer 6, bypassing both layers 7 and 8. *Chimney SW1* was first discovered in 2008 when a second accumulation in Layer 8 started developing seemingly unconnected to the initial Layer 8. First, it was believed that the two accumulations in Layer 8 was connected, and the second accumulation was a result of lateral migration via a passage too thin to be observed. However, the southernmost accumulation continue to grow separately from the northern accumulation, and by the time of the 2016 dataset (the most recent survey) the northern and southern accumulation have not merged.

Reservoir simulations of the CO_2 plume has either been based on migration through the shales after threshold pressure is exceeded (Cavanagh and Haszeldine, 2014) or physical disturbance of the shales create pathways for vertical migration (Chadwick et al., 2004b). In this work the main objective is to create flow pathways through the intra-shales and establish the affects of these feeders on the plume, and from this to improve the geological interpretation.

Chapter 3

Theory

3.1 Carbon Dioxide Properties

Carbon dioxide is a triatomic compound with chemical composition CO_2. The molecule is symmetrical and non-polar. Carbon dioxide in gas phase is colorless, and have a faint sharp odour and sour taste. CO_2 is a minor part of the atmosphere, only about 0.04% (other components of the atmosphere, 78% Nitrogen, 21% Oxygen, 0.9% Argon), but is one of the most important greenhouse gases linked to global warming. CO_2 produce the greenhouse effect by keeping some of the radiant energy received by the Earth from being returned to space (Encyclopaedia Britannica). Carbon dioxide changes phase based on temperature and pressure, Figure 3.1. Carbon dioxide in gas phase is a clear, colorlesss and odorless. CO_2 in supercritical phase have high density, like a liquid, and low viscosity, like vapour, and occur at 7.38 MPa and $31.1°C$. These temperature and pressure conditions generally occur at 800 meter depth in the subsurface. CO_2 is slightly soluble in water, 1.79 volumes per volume at $0°C$ and atmospheric pressure, larger amounts at higher pressure, forming a weakly acidic solution (Encyclopaedia Britannica).

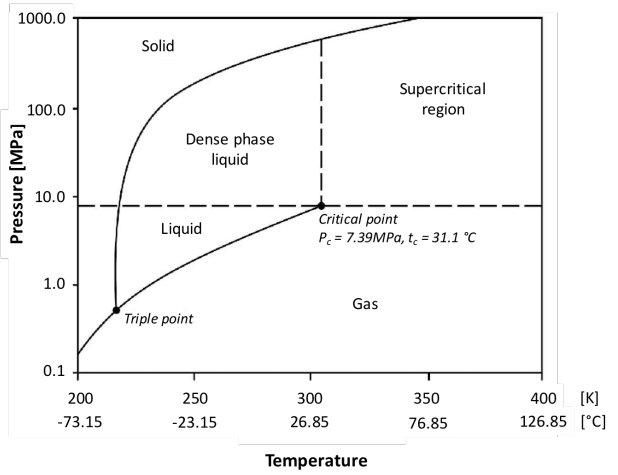

Figure 3.1: Phase diagram for CO_2. Modified from Witkowski et al. (2014).

3.2 Permeability

Permeability, k, is a measure of how well a porous media conducts/ transmits fluids, and is expressed by Darcy [D] and Darcy's law.

$$Q = \frac{kA\Delta P}{\mu L} \tag{3.1}$$

Darcy's law here expressed through Q, flow rate; A, cross-sectional area; P, differential pressure across core; μ, viscosity; L, length. Darcy's law assume laminar flow, steady state flow, isothermal conditions, incompressible fluid, homogeneous formation, non reactive fluid and single phase. One darcy describes the permeability of a porous medium through which the passage of one cubic centimeter of fluid having one centipoise of viscosity flowing in one second under a pressure differential of one atmosphere where the porous medium has a cross- sectional area of one square centimeter and a length of one centimeter.

In reservoir engineering one differentiate between absolute permeability, effective permeability and relative permeability. The absolute permeability is an expression of the intrinsic permeability of the rock itself, the property of the rock alone and not the fluid that flows. Thus, with the assumption that no chemical reactions take place between the rock and the flowing fluid. It is measured by flowing a single fluid through the rock. The absolute permeability will be constant no matter what type of fluid is flowed through the rock.

Effective permeability is the permeability of one fluid flowing through the rock when there are other immiscible fluids present in the rock. The effective permeability is not constant, and will vary depending on the saturation ratios of the fluids.

Relative permeability is the ratio of the effective permeability of one fluid at a particular saturation to the absolute permeability of that fluid at 100% saturation. The term drainage describe when the saturation of the wetting fluid, Section 3.3, of the rock decrease, while imbibition describe increase in saturation of the wetting fluid, Figure 3.2.

3.2.1 Upscaling Flow Properties

Upscaled permeability refers to the permeability of a larger volume given some fine scale observations or measurements. In reality, the permeability in a rock medium is a highly variable property, with a general decrease from surface to depth due to compaction and diagenesis. Due to the highly variable nature of permeability averaging is generally necessary in estimating the effective permeability used in reservoir modelling. In ideal systems the general practice is to use the arithmetic average, Equation 3.2, for flow along continuous parallel layers, while flow perpendicular to continuous parallel layers the harmonic average, Equation 3.3, is used. For more variable rock systems the geometric average, Equation 3.4, is often proposed as a solution (Ringrose and Bentley, 2015).

Arithmetic mean:

$$\bar{X}_{arithmetic} = \frac{1}{n}\sum_{i=1}^{n} x_i \tag{3.2}$$

Harmonic mean:

$$\bar{X}_{harmonic} = \frac{1}{\frac{1}{n}\sum_{i=1}^{n}\frac{1}{x_i}} \tag{3.3}$$

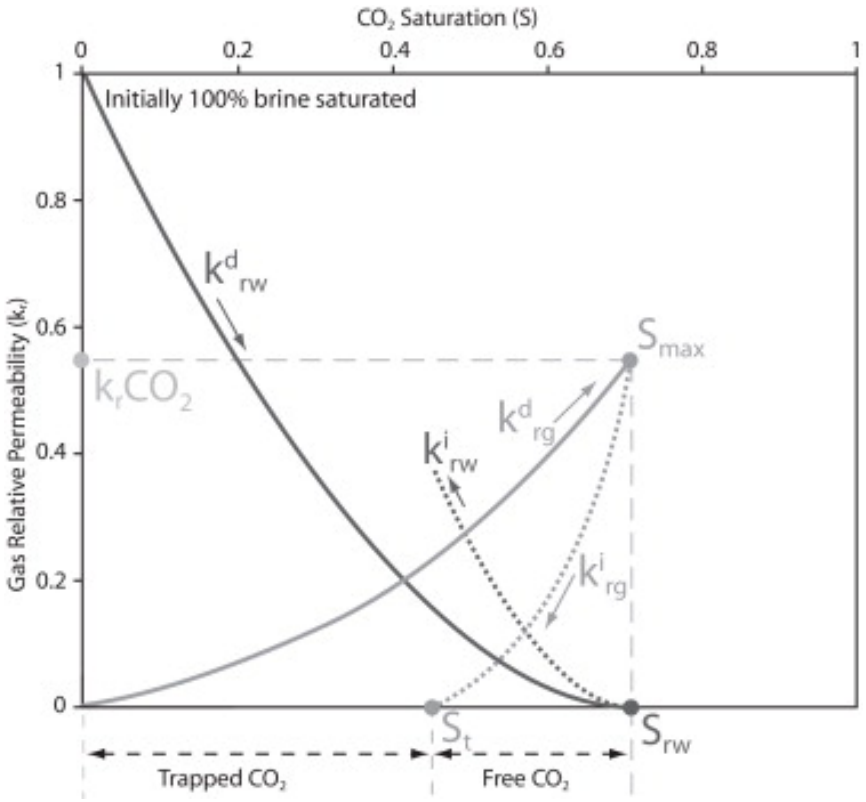

Figure 3.2: An example of relative permeability curves for CO_2 and brine. Initially the rock core samples are 100% saturated in brine, during drainage the brine saturation decrease and follow the relative permebility curve for brine, k^d_{rw}. While CO_2 saturation increase and the gas permeability follows the relative permeability drainage curve of gas, k^d_{rg}, with S_{max}, maximum saturation, as end point. The maximum saturation of CO_2 is obtained when brine relative saturation is reached, S_rw, and brine relative permeability equals zero. The dotted lines represent imbibition scenario, where brine is injected back into the core sample, CO_2 decreases along the imbibition curve, k^i_{rg}. When CO_2 permeability equals zero no more CO_2 can be displaced from the pore space and the residual or trapped gas saturation, S_t, is reached (Burnside and Naylor, 2014).

Geometric mean:

$$\bar{X}_{geometric} = \sqrt[n]{x_1 x_2 x_3 ... x_n} \tag{3.4}$$

3.3 Wettability

Wettability is defined as the tendency for one fluid to be preferentially attracted to a solid surface rather than another. Adhesion tension, A_t, is a function of interfacial tension and contact angle, and determines which fluid will wet the surface (Ahr, 2008).

$$A_t = \sigma_{so} - \sigma_{sw} = \sigma_{wo} \cos(\theta_{wo}) \tag{3.5}$$

σ_{so}, IFT between solid and lighter fluid (oil); σ_{so}, IFT between solid and denser fluid (water); σ_{wo}, IFT between the two fluids; θ, angle between σ_{sw} and σ_{wo}, illustrated in Figure 3.3. The wettability conditions rage from totally water wet ($\theta = 0°$), water wet ($\theta < 90°$), neutrally wet ($\theta = 90°$) and oil wet ($\theta > 90°$).

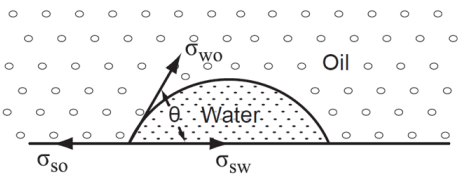

Figure 3.3: Illustration from Ahr (2008). The IFT values, σ, and contact angle, θ, between two liquids in a oil/water system with a solid surface.

The wettability is depended on the reservoir material and pore geometry, and geological mechanisms. As well as the composition amount of different fluids and the pressure and temperature. Mechanisms occurring during injection or production, i.e. change in saturations, pressure and composition.

The wettability determines the fluid distribution in the reservoir and the continuity of the wetting phase.

3.4 Fluid Forces and Plume Migration Regimes

Gravity-, viscous-, and capillary-dominated fluid flow are the end members of the fluid force system. Gravity dominated flow is dominated by gravity and the buoyancy effect. Capillary dominated fluid flow is dominated by the capillary forces. The interplay of forces (viscous, capillary and gravity) in reservoir models is commonly defined using scaling-group theory.

When injecting CO_2 into a storage reservoir, viscous forces dominate flow behaviour in the near wellbore region due to high injection rates and large pressure gradients. In the viscous flow regime the CO_2 moves as a compact front, flooding all the pores it encounters in the rock, and saturations in the near wellbore region is depended on the spatial permeability in the formation. As CO_2 migrate farther from the injection point, the velocity and pressure gradient decrease until it becomes negligible compared to the buoyancy and capillary forces (Ganesh et al., 2013).

3.4.1 Capillary Pressure

Capillary pressure can be thought of as the force necessary to drive a non-wetting fluid through pores already saturated with a wetting fluid. It occurs when two immiscible fluids are present in a porous medium, and can be expressed as the pressure differential across the fluid interface, given that the fluids are in equilibrium and not flowing, Eq. 3.6.

$$P_c = P_{non-wettingphase} - P_{wettingphase} = \Delta\rho gh \tag{3.6}$$

Capillary pressure can also be expressed in terms of surface forces, by balance the upward and downward forces, Eq. 3.7. Rearranging

$$2\pi r A_t = \pi r^2 \Delta\rho gh \tag{3.7}$$

For sheet-like pore throats, the capillary pressure equation, according to Wardlaw (1976) , is more realistically written, Eq. 3.8 (Ahr, 2008).

$$P_c = \frac{\sigma_{wo}\cos\theta_{wo}}{r} \tag{3.8}$$

3.4.2 Threshold Pressure

Threshold diplacement pressure is defined as the minimum pressure needed to initiate the displacement of a wetting phase by a nonwetting phase from a porous medium fully saturated with the wetting phase (Thomas et al., 1968):

$$P_{th} = \frac{2\sigma\cos\theta}{r} \tag{3.9}$$

P_{th}, threshold pressure expressed by σ, IFT between the invading phase and resident phase; θ, the wetting angle between the invading phase and the rock; r, the representative pore throat radius for the rock.

One can define the breakthrough condition to be the pressure where the upward force of the CO_2 column equals, or exceeds, the threshold pressure of the rock, Equation 3.10.

$$\Delta\rho gh = \frac{2\sigma\cos\theta}{r} \tag{3.10}$$

3.4.3 Trapping Mechanisms

The subsurface trapping mechanisms of CO_2 involve both physical and geochemical factors, and can be divided into 4 mechanisms: (1) structural and stratigraphic trapping, (2) residual CO_2 trapping, (3) solubility trapping and (4) mineral trapping (Krevor et al., 2015).

The structural and stratigraphic trapping is governed by the buoyancy effect and the capillary forces. The caprock the capillary entry pressure is high, and that will result in a column of CO_2 supported by the caprock.

When CO_2 is injected, it is injected deep in the formation. The lighter density of the CO_2, will raise from the injection point to the top of the structure due to the density

difference between the brine and the CO_2. Along the migration pathway CO_2 will be capillary trapped in the pores of the reservoir as residual CO_2. By injecting at the bottom of the reservoir, the amount of CO_2 that dissolved in the brine also is maximized.

CO_2 also react with the brine in the formation, creating a solution that is more dense than brine. This is believed to result convective mixing. The convection can only occur if the a certain amount of CO_2 has been dissolved in the brine, and the top diffusive boundary layer need to achieve a critical thickness before convection occur. The critical time for convection to happen is estimated to be in the range of: 10 days to 2000 years. This trapping mechanism is an effect that would assist and stabilize long term storage, as one over time would have less free CO_2 in the reservoir that could escape to the surface.

3.5 Monitoring

When injecting CO_2 into the subsurface there is always a risk of leakage. In the subsurface there are several different leakage pathways, some possible being fault zones, fractures, sand injectites and the well itself. Site selection and mapping is of the outmost importance to limit the risk of leakage, but these risk factors can only be mapped and "described" to a certain extent. Currently there are no standard protocols or established designs for CO_2 monitoring. Each storage project must therefore design its own fit-for-purpose monitoring program. The design of the monitoring program will depend on the objective and requirements of the site, the degree of risk of leakage.

A CO_2 monitoring portfolio should ensure safe site operation, satisfy regulatory requirements, secure long term storage of CO_2 and address possible public concerns about possible leakage.

Monitoring objectives fall into three main categories: (1) conformance; ensuring the behaviour of CO_2 in the reservoir is understood. (2) containment; ensure that CO_2 stays within the storage unit. (3) contingency; the ability to respond to anomalies and potential leakage events.

3.5.1 4D Seismic Data

From a monitoring perspective seismic data is perfect to ensure conformance and containment.

Seismic Response

As a seismic wave propagates the Earth, the velocity can be expressed as a function of bulk modulus, K, shear modulus, G, and the bulk density, ρ_{bulk} given Equation 3.13. Compressional wave velocity in isotropic medium given by Equation 3.11. The compressional wave is often referred to as the p-wave or the primary wave.

$$V_P = \sqrt{\frac{K + \frac{4}{3}G}{\rho_{bulk}}} \tag{3.11}$$

Shear wave velocity, not dependent on the bulk modulus, K. The shear wave is often referred to as the secondary or S-wave given by Equation 3.12.

$$V_S = \sqrt{\frac{G}{\rho_{bulk}}} \tag{3.12}$$

Bulk density, a function of porosity, ϕ, density of fluid, ρ_{fluid}, and density of rock/solid, ρ_{solid}. Density of solid can be expressed as the sum of the solid phases with fractions, f_i:

$$\rho_{bulk} = \phi\rho_{fluid} + (1-\phi)\rho_{solid} = \phi\rho_{fluid} + \sum_{i=1}^{n}(1-\phi)f_i\rho_{solid,i} \tag{3.13}$$

Reflection coefficient:

$$RC = \frac{\rho_2 V_2 - \rho_1 V_1}{\rho_2 V_2 + \rho_1 V_1} \tag{3.14}$$

When CO_2 substitute brine in the reservoir, a strong sonic velocity contrast between the CO_2 and the native brine is created.

The resolution of the reflections from the top and bottom of a bed is dependent on the interaction of closely spaced wavelets. The vertical resolution has two limits, the limit of separation and limit of visibility. The limit of separability, Eq. 3.15, is simply the bed thickness corresponding to the closest separation of the two wavelets, and is equal to one-quarter of a wavelength (or half a period). For beds thinner than this is still visible, but the top and base reflections are progressively attenuated until the limit of visibility is reached. This is when the signal becomes obscured by background noise. The limit of visibility is a variable fraction of the wavelet, and depends on the acoustic contrast of the layer, the noise in the data, both random and systematic, and the phase of the seismic wavelet (Brown, 2011)

$$Limit\_of\_separability = \frac{\lambda}{4} \tag{3.15}$$

Feeder Chimneys

Furre et al. (2019) define the feeder chimney as a vertical feature of disturbed or dimmed amplitudes.

3.5.2 Other Monitoring Techniques

- **4D Gravity monitoring** - Conformance and containment - High precision gravity monitoring offers an independent measurement of density, and in the case of CO_2-injection; a measurement of saturation. Because density is linearly related to saturation (Furre et al., 2017).
- **CSEM** - Remote-sensing technology to map the electric resitivity distribution of the subsurface.
- **Microseismic** - Passive observations of small-scale seismic events.
- **Satellite (InSAR)** - Remote sensing. Extremely valuable and cost effective monitoring of onshore CO_2 storage sites.

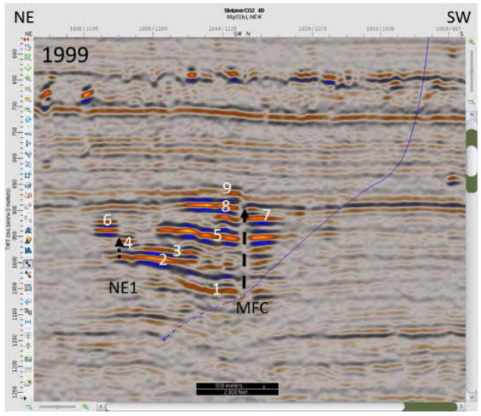

Figure 3.4: From Furre et al. (2019). Interpretation of 9 layers, and MFC as a vertical feature of dimmed amplitudes, and the NE1 feeder which is not visible, but implied from offset layer growth.

3.6 Geological Reservoir Modeling

3.6.1 Shallow Marine Sandstone Reservoirs

Shallow marine sandstone reservoirs are one of the few reservoir types to occasionally behave like 'tanks of sand'. Shallow marine reservoirs are generally laterally continuous, sand rich and well sorted, and have from deposition a positive interaction between flow processes and geology. However, shallow marine reservoirs are varied and can contain important heterogeneites not visible on the seismic scale or log scale, and could also be poorly sampled in core data. In wave-dominated shallow marine settings heterogeneties usually derive from fine scale laminations. Laminations can be a result of either wave-related oscillatory currents at the seabed or unidirectional currents resulting in swaley or hummocky cross stratified lithofacies. These heterogeneties make a significant contribution to flow heterogeneity (Ringrose and Bentley, 2015).

3.6.2 Net Definitions

Net sand, clean sedimentary rock. **Net reservoir**, net sand intervals with useful reservoir properties. **Net-to-gross**, should be used with reference to one of the above, eg "N/G reservoir".

3.7 Geology

3.7.1 Shallow Marine Sands

Offhore from most coastlines there is a region of shallow water, the continential shelf, before the water deepens down to abyssal depths. The continential shelf can stretch tens to hundreds of km out to sea. Ocean basins do not separate all land areas, but land is instead

separated by shallow, epicontinential seas. In these shallow marine environments terrigenous clastic material is brought in by rivers from the continential realm, and distributed by tides, waves, storms and ocean currents. The highest concentration of clastic input are near the mouths of major rivers, and sediments will be redistributed to adjacent coastal regions by longshore movement of materials by waves, storms and tides. Shallow marine environments are (Nichols, 2009).

3.7.2 Low-stand Fan

A low-stand fan deposits, also referred to as basin-floor fan, occur in an interval of low sea level, called a low-stand. The sea level rise slowly, but sediment supply is relatively high. The shelf is bypassed and sedimentation occur on the basin floor as turbidites. At the base of the slope, above the fan, sediments also start building up forming a low-stand wedge. In these deposits the pattern of the beds are initially progradational, and becoming aggragational in the low-stand wedge as the rate of sea level increases (Nichols, 2009).

3.7.3 Sand Injectites

Sand injectites are created by a post-depositional process where fluidized sand is remobilized and injected into the stratigraphy. A range of geometries are exhibited by sand intrusions and remobilized sandstones, but can be broadly subdivided into four elements: parent units, dikes, sills and extrudites. The parent units are depositional sandstones that display features formed both by depositional processes and post-depositional sand and fluid mobilization, and form an interconnected system of sandstones together with sandstone intrusions. Sand injectites are typically fine- to medium-grained siliciclastic sand, although much coarser and carbonate sand examples do occur. Outcrop and petrographic data indicate that sandstone intrusions act as high-permeability conduits for the migration of fluids. There are limited published porosity and permeability data of sand injectites, the two properties impart control the storage and flow capacity of rocks. To date, no outcrop studies of permeability are published and only two core-based studies have examined the permeability characteristics of injected sandstones. Sandstone intrusions show a slight reduction in mean permeability when compared to the parent rock, but the permeability distribution is broader in the parent rock than the sandstone intrusions. This change in permeability distribution has been attributed to the process of sand remobilization where the internal sedimentary structures of the parent unit is destroyed during sand fluidization, creating a more isotropic and homogeneous microtexture of the injected sand. (Hurst et al., 2011).

Figure 3.5: Sand injectite in outcrop at Deltaneset, Svalbard. Book for scale. Photo: private.

Chapter 4

Experiment

4.1 Data

4.1.1 The Sleipner 2019 Benchmark Model

The Sleipner 2019 Benchmark Model is released by Equinor in 2020, and freely avaliable online as through CO2 DataShare, published via SINTEF on behalf of the CSDC project (CO_2 Storage Data Consortium).

The Sleipner 2019 Benchmark model is a 3D volume include the storage aquifer and the caprock lateral extent is 3.2km by 5.9km. Thickness varies, but up to 300meters. Lateral resolution defined as 50m by 50m, vertical resolution defined as about 2m, while the vertical resolution of the intra-shale cells is about 0.5m and caprock cells is 5m.

The model consist of nine sandstone layers, Utsira L1 to Utsira L9. Utsira L1 to L8 are separated by thin, low permeability intra-shale layers of about 1m, L8 and L9 are separated by a thicker shale layer of 7m, referred to as "Thick Shale Unit". In the model the caprock is defined as a shale unit of constant thickness of 50m. In reality the shale is much thicker.

The grid properties for porosity and permeability are the same as used in the 2011 benchmark model, Table 4.1.

In the reference dataset two wells, 15/9-A-16 and 15/9-13, are included. 15/9-13 is an exploration well, while 15/9-A-16 is the injection well for the CO_2 storage operation at Sleipner. Boundary polygons of the CO_2 distribution outlines of each internal sandstone layer, L1 - L9, are provided for 2010. With a lateral grid resolution of 50m x 50m, Figure 4.2, (Equinor, a).

Feeders

Three feeders, interlayer leakage points, are represented in the Benchmark Model and represented by polygons. These three feeders include: *Main Feeder Chimney*, *North-eastern feeder* and *South-western feeder*.

Model parameter	Symbol	Unit	Reference Value	Range
Caprock				
Porosity	ϕ_{cap}	%	35	34-36
Permeability	k_{cap}	mD	0.001	0.00075 - 0.0015
Utsira Fm				
Porosity	ϕ_{res}	%	36	27-40
Permeability	k_{res}	mD	2000	1100 - 5000
Intra-shale				
Porosity	ϕ_{sh}	%	34	31-38
Permeability	k_{sh}	mD	0.0010	0.00075 - 0.0015

Table 4.1: Sleipner Reference Model Input Parameters (Equinor, a)

The Main Feeder Polygon, can be directly interpreted on the seismic data, and is observed at all acquisition times, and through all layers.
North-eastern feeder, Layer 5 to Layer 6, poorly constrained with lower confidence, not directly observed on seismic, but derived from enhanced amplitudes in Layer 6, and lateral development of Layer 5.
South-western feeder, Layer 7 to Layer 8, poorly constrained with lower confidence, not directly observed on seismic, but derived from the 2008 observation of enhanced amplitudes in Layer 8 and extent of Layer 7.

4.2 Modeling Procedure

Schulmberger's ECLIPSE consists of two separate simulators; ECLIPSE 100 specializing in black oil modeling and ECLIPSE 300 specializing in compositional modeling. ECLIPSE 300 was used modelling the CO_2 injection into the Utsira Fm.

Utilizing the CO2STORE option in Eclipse, three phases are considered, a CO_2 rich phase, an H_2O rich phase and a solid phase. Where the CO_2 rich phase is labeled the gas phase, and the H_2O rich phase is labeled the aqueous phase (liquid phase). The mutual solubilities of CO_2 and H_2O are calculated to match experimental data for CO_2- H_2O systems under typical CO_2 storage conditions; $12 - 100°C$ and up to 600bar (60 MPa).

4.2.1 Input Parameters and Modelling Geological Features

To improve the implications of the feeders identified two geological features are included in the modelling procedure. The size and location of these features are edited to both get a better fit for the observed plume, and to illustrate different geological scenarios.

Modelling geological features are achieved by editing the properties of the intra-reservoir shales. In this work two types of vertical features are investigated; Zones of high permeability sand in the shales and high permeable flow pathway with restricted horizontal permeability.

Model parameter	Symbol	Unit	Reference Value
Caprock			
Porosity	ϕ_{cap}	%	35
Permeability	k_{cap}	mD	0.001
Utsira Fm			
Porosity	ϕ_{res}	%	36
Permeability	k_{res}	mD	2000
Intra-shale			
Porosity	ϕ_{sh}	%	34
Permeability	k_{sh}	mD	0.0010

Table 4.2: Input Parameters. Utsira Fm and Caprock properties similar to The Sleipner 2019 Benchmark Model (Equinor, a)

Aquifer support is included in the model by multiplying the pore volume at the model limits.

Sand zones in shales

By populating the cells in the shales with the same properties as the reservoir sand, geological features with good flow communication between the sand bodies and the flow pathway is achieved, Figure 4.1a. This can also be described as creating holes in the intra-reservoir shale barriers. This can represent patchy shale layers, where there is zones of non-deposition of shale, or zones of erosion.

Reduced horizontal permeability

The second geological feature included is a vertical high permeable sand feature with decreased horizontal permeability. This can represent discontinuous shales and lateral flow heterogeneties in the sands or a sand injectite, Figure 4.1b. The horizontal permeability, k_h and k_v, is set to 500 mD, a quarter of the permeability of the sand in the storage reservoir.

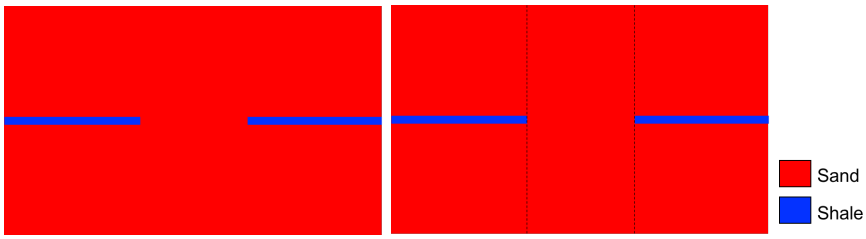

(a) Non-continuous shale layers. Could represent a number of geological scenarios depending on distribution.

(b) High permeable flow pathway with restricted horizontal permeability, vertical lines to represent reduced connectivity between the vertical feature and reservoir sand bodies.

Figure 4.1: Illustrations of geological features used in simulations.

4.2.2 Well Placement

The first step in the modelling procedure was to ensure proper well placement, and injection zone.

The injection well 15/9-A-16 is a deviated well. Injection depth is described as 1010m, which according to the well trajectory is located at E 438438.08, N 6471250.53. In the model this correspond approximately to cell X:31 Y:42 and Z:215-217, where a vertical well is placed for simplicity, Figure 4.2.

The well inject 1 423 400 Sm^3/day (2750 tonnes/day) which corresponds to 1Mt/year (Eiken et al., 2011), calculation in Appendix A.1. All simulations will be preformed with the same time steps, simulation starting at 15. September 1996, time= 0, before monthly time steps from 1. January 1997 to 1. December 2010, and the well shut-in 1. January 2011.

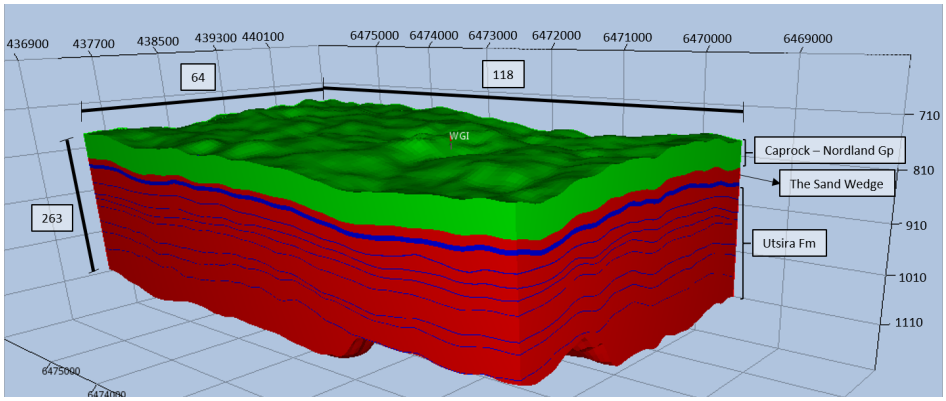

Figure 4.2: The Sleipner Benchmark Model visualized in ResInsight, green caprock, red reservoir sand and blue intra-shale. The model is 64x118x263 cells. Depth in meters on the z-axis. Figures are always shown with vertical exaggeration of 5, z=5. WGI representing the injection well.

4.2.3 Modelling cases

The property of the lithologies are kept constant, and the values used are the reference values from The Sleipner 2019 Benchmark Model, Table 4.2.

Basecase: Permeable Barriers Input

As a basecase in the modelling process, the Benchmark model is utilized with the values presented in The Sleipner 2019 Benchmark Model, but without the feeders. In other words, the intra-shale barriers are laterally continuous.

Case 1: All-Sand Input

Next, a simulation of an homogeneous sand reservoir is preformed. The objective of this simulation is to establish flow behaviour without intra-reservoir flow barriers, and thus,

CO_2 arrival at the top of the reservoir without barriers.

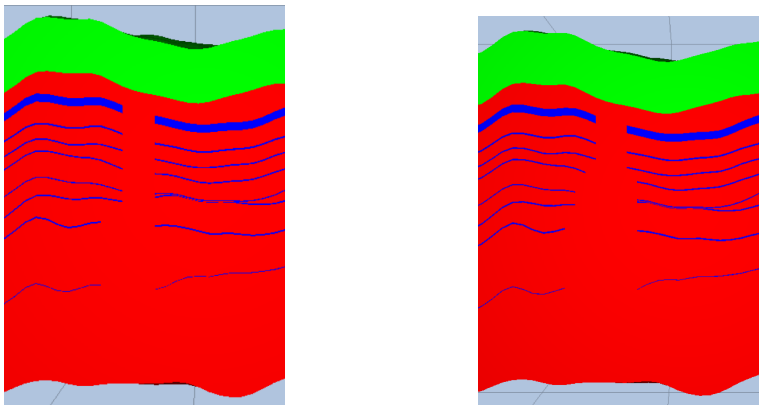

(a) CASE 2.2.1 MFC becoming wider at depth.

(b) CASE 2.2.2 MFC gradually becoming wider with depth.

Figure 4.3: Cross section of the MFC.

Case 2: Barriers with MFC

Further, the second case, similar to the basecase, but with a zone with sand properties working as a migration pathway through the intra-shales, representing the MFC. According to Furre et al. (2019) the MFC measure between 50-190 meters across in the upper part of the plume. Locations for each sub-case in Table 4.3.

Case 2.1: Barriers with small MFC In Case 2.1 the size of the vertical migration path is modelled with 1x1 cell, or 50x50 meter, representing the lower approximation of the MFC.

Case 2.1.1: Small MFC, first, the small MFC is placed directly above the injection point.

Case 2.1.2: Small MFC, displaced, secondly, the small MFC is displaced from the injection point, in SW direction. The objective of this case is to investigate how the placement of the MFC affect top arrival of the CO_2.

Case 2.2: Barriers with large MFC, next, the size of the MCF is changed to 3x2, or 150x100 meter, where the diagonal is 180.3 meter. This represent the bigger approximation of the MFC.

Case 2.2.1: Large MFC, first, the large approximation of the MFC is placed directly above the injection point.

Case 2.2.2: Large MFC, Displaced, secondly the large MFC is displaced from the injection point, and is placed SW of injection point. Similar to Case 2.1.2 is the objective of this iteration how the placement of the MFC affect top arrival of the CO_2.

Case 2.3: MFC Increasing in Size Furre et al. (2019) points out that the MCF appears to be wider in the deeper part of the time section. Two different scenarios were tested; one with one change in size and another with two changes in size.

Case 2.3.1: MFC Increasing Size Version 1, the first simulation with a MFC increasing in size downward, the top six intra-reservoir shale layers have a 2x2 cells, 100x100m, feeder. While the bottom two intra-reservoir shale layers are 5x5 cells, 250x250m.

Case 2.3.2: MFC Increasing Size Version 2, the second simulation adds a middle part to the feeder of intermediate size.

Case 2.4: MFC with restricted horizontal permeability The MFC is also represented by geological feature with restricted horizontal permeability, Figure 4.4

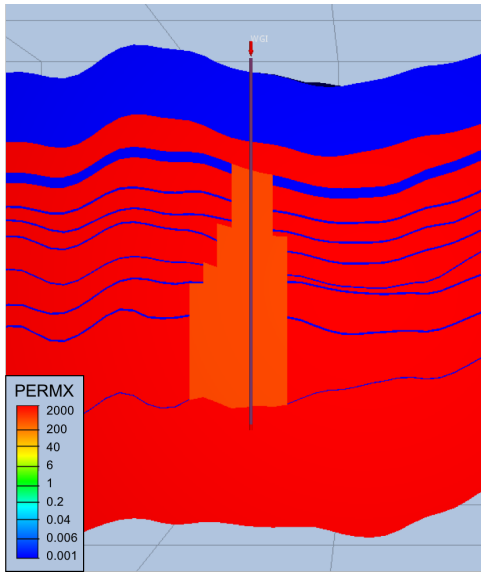

Figure 4.4: Horizontal permeability of MFC with reduced permeability. On figure x-permeability, similar for y-permeability.

X	Y	Z
Small MFC		
31-31	42-42	32-205
Large MFC		
30-32	41-43	32-205
MFC Increasing Size Version 1		
30-32	41-43	32-150
30-35	41-45	150-205
MFC Increasing Size Version 2		
30-32	41-43	32-90
30-33	40-44	90-120
30-34	40-45	120-150
30-35	40-46	150-205

Table 4.3: Locations of the MFC in the different cases.

Case 3: Barriers with MFC and Feeders

The MFC case used further to add feeders is the Case 2.3.2: MFC with variable size. The layer developed was different in the simulation compared to what is observed in the seismic interpretation. Considering the objective to explore the implications of different geological features on the plume, the feeders are placed in the direction of what they are observed, but at the plume development in the simulation at the time they first were identified.

The NE1 feeder, the first feeder, was identified already at the first seismic time-lapse survey after injection, acquired October 1999, about 800m from the injection point. The feeder is believed to source Layer 6 from Layer 5. In the model this feeder is placed based on Layer 5 development January 1999. Location that was chosen was [36 47 95-105], this is only 350m from the injection well.

The SW1 feeder was first identified in 2008 when a second accumulation in Layer 8 started growing separately from the initial Layer 8. The proposed theory is that the second, Southern, accumulation in Layer 8 is sourced from Layer 5, bypassing 6 and 7, to Layer 8 (Furre et al., 2019). The placement of the SW1 feeder is decided from the Layer 5 development in June 2007, a year before the 2008 seismic survey was acquired, and a year after the 2006 survey where no separate Layer was seen. The SW1 Feeder is described to be located 1000m SW of the injection point. Layer 5 in the simulation does not extend far to the SW, and the SW1 feeder was placed more South of the injection point, location [34 36 57-105], 365m from the injection point.

Case 3.1: Feeders, the feeders are first represented as sandy holes in the shales, without restricted permeability.

Case 3.2: Feeders with restricted horizontal permeability, before being represented by restricted horizontal permeability.

4.3 Sleipner 4D Seismic Dataset

This dataset contains processed 4D seismic cubes from 1994 - 2010.

Survey	ST9407	ST9906	ST0106	ST0403	ST0607	ST0814	ST10018
Date Aquired	6/8/94-10/9/94	8/10/99-10/10/99	27/9/01-1/10/01	13/6/04-13/8/04	2/6/06-20/6/06	4/5/08-15/6/08	15/10/10-17/10/10

Table 4.4: Overview of seismic datasets and aquisition date (Equinor, b).

Surveys until and including 2001 processing were preformed by WesternGeco (p01). A full reprocessing was conducted in 2007 (p07) by PGS on the seismic data from 1994 and 2001, in addition to the 2004 and 2006 data. The time-lapse processings in 2008 and 2010 were carried out similar to the 2007 processing sequence, but a final matching to the 1994 data was required, therefore we have separate vintages for 1994 reprocessed in 2008 and 2010 too. The 2010 data went through both a time-lapse and an imaging route, Table 4.5, (Equinor, b). The acquisition dates are used to give best possible comparison with the simulations from Eclipse. The seismic lines used in the quantitative comparison was chosen based on the location across the plume.

4.3.1 Interpretation

The goal of the seismic interpretation is to identify the CO_2 layers, and the top plume geometry. The interpretation is done in Schlumberger Petrel.

Vintage	Processing	Comment
94	p01	Time-lapse processed
94	p07	Time-lapse processed
94	p08	Time-lapse processed
94	p10	Time-lapse processed
99	p01	Time-lapse processed
01	p01	Time-lapse processed
01	p07	Time-lapse processed
04	p07	Time-lapse processed
06	p07	Time-lapse processed
08	p08	Time-lapse processed
10	p10	Time-lapse processed
10	p11	Image processed

Table 4.5: Overview of seismic data vintage and processing.

Chapter 5

Results and Interpretation

5.1 Eclipse Modelling Results

5.1.1 Base Case

The step-wise development on a yearly basis in Appendix A.2. From the step-wise development it can be observed that the CO_2 plume, displayed as CO_2 saturation/gas-saturation, is contained under the lowest intra-reservoir shale layer, and over time expand as more CO_2 is injected. In the base case the CO_2 does not reach the top of Utsira, and the Sand Wedge, but is contained under the lowermost intra-reservoir shale.

5.1.2 Case 1: All Sand, No Barriers

The step-wise development on a yearly basis in Appendix A.3. From the step-wise development it can be observed that the CO_2 plume forms a cone shape as it migrate towards the caprock, which it reaches October, 1998. With no barriers in the reservoir there a subsequently no layering of the plume in the model, Figure 5.8.

The top plume geometry of case 1 with all sand can be described as elliptical, Figure 5.1a, with a width of 2817 meters in East-West direction, 3592 meters in North-South direction, and 4190 meters across. The top follow the geometry of the caprock.

5.1.3 Case 2.1: MFC, Small

The step-wise development on a yearly basis in Appendix A.4. The step-wise development shows how the CO_2 migrate through the vertical pathway, and further migrate laterally under the intra-reservoir shales creating a layered plume over time.

The Layering of the plume with a small MFC results in a plume with a laterally extensive CO_2 layer in L1 and the following layers decrease in size upward, Figure 5.9.

Top arrival. The small MFC was simulated twice; first time with the vertical pathway directly over the injection point, secondly with a displaced vertical migration pathway.

Placing the MFC directly above the injection point resulted in the same top arrival of CO_2 as Case 1, October 1998. While a displaced MFC resulted in CO_2 top arrival later, January 1999, Figure 5.12 and Figure 5.13.

Top plume geometry. A MFC with a width of the smaller approximation results in a top plume which is 1500m across, and 1110m from southernmost point to the northernmost point, Figure 5.2. The layer follow the geometry of the caprock, and is constrained in an anticlinal feature.

5.1.4 Case 2.2: MFC, Large

The step-wise development on a yearly basis in Appendix A.5. Similar to Case 2.1 the CO_2 migrate vertically and spread out beneath the intra-reservoir shales. The difference is the distribution of CO_2, where bigger MFC distribute the CO_2 more equally in the reservoir resulting in more evenly sized intra layers. Similar to case 2.1, small MFC, the large MFC was simulated twice; once with MFC directly over the injection point, secondly with a displacement.

The top arrival of the CO_2 is interpreted to reach the caprock in September and spread out laterally under the caprock by 1. October 1998 with the feeder placed directly over the injection point, Figure 5.14. However, with a displacement the CO_2 arrives later, and is interpreted to arrive at the caprock by December 1998, and spread out laterally January 1999, Figure 5.15.

Layering, with a bigger MFC the layers develop equally, resulting in similar lateral extent of each layer.

Top plume geometry, with the large MFC layer 9 is measure 2285 meter West - East, 2200 meter North-South, and 2110 meter across, Figure 5.3. Significantly bigger than the top plume with small MFC.

5.1.5 Case 2.4: MFC with Reduced Horizontal Permeability

The step-wise development on a yearly basis in Appendix A.6. From the step-wise development it can be observed that the CO_2 stay in the MFC, before layer development happens. The layers initially develop with similar extent, before the geometry of each individual intra-shale govern the further geometry for each layer.

The resulting **layering** in 2010, the top layer is the largest, and layer 4 the smallest.

Top arrival of the CO_2 is July 1998. The interpretation of this is that the reduced horizontal permeability result in the CO_2 prefer to migrate vertically. Resulting in the earliest top arrival of the simulations.

Top plume geometry is similar to the previous iterations with the MFC, but slightly different measurements. The top plume measure 2305m East-West direction, 2462m North-South direction and 2425 across, Figure 5.5.

5.1.6 Case 3: MFC with Feeders

Case 3.1: MFC with Feeders The locations of the feeders were decided on by the extent of layer 5 January 1999 for NE1 feeder and Y for SW1 feeder. The NE1 feeder starts to distribute CO_2 to Layer 6 by January 1999, and reaches the top of Layer 6 in April 1999,

Figure 5.16. At the same time the layer 6 CO_2 migrate laterally to join the CO_2 distributed from the underlying layer. Resulting in one accumulation sourced by both the MFC and the NE1 feeder. On the other hand, the SW1 feeder was placed based on the Layer 5 extent January 2007, but due to the NE1 feeder the extent of the layer is changed, and the CO_2 never reaches this location in the simulation. However, the CO_2 in the overlaying layer 6 starts to migrate into the feeder already in November 1999, and reaches Layer 7 August 2000, and Layer 8 by October 2001.

Case 3.2: MFC with reduced horizontal permeability feeders similar to Case 3.1, but with reduced horizontal permeability, like described in Section 4.2.1. Similar to the previous case, Case 3.1, the CO_2 does not extend to the cell of the SW1 feeder in Layer 5, and the feeder is sourced by Layer 6. **Top plume geometry**, between the two different cases of feeders with different properties, the differences in top plume geometry is minimal. Case 3.1 measuring 2280m East-West, 2370m North-South and 2325m across, while Case 3.2 measure 2270m East-West, 2380m North-South and 2295m across. **Top plume arrival** of each of the cases are both September 1998.

5.1.7 Top Plume Geometry

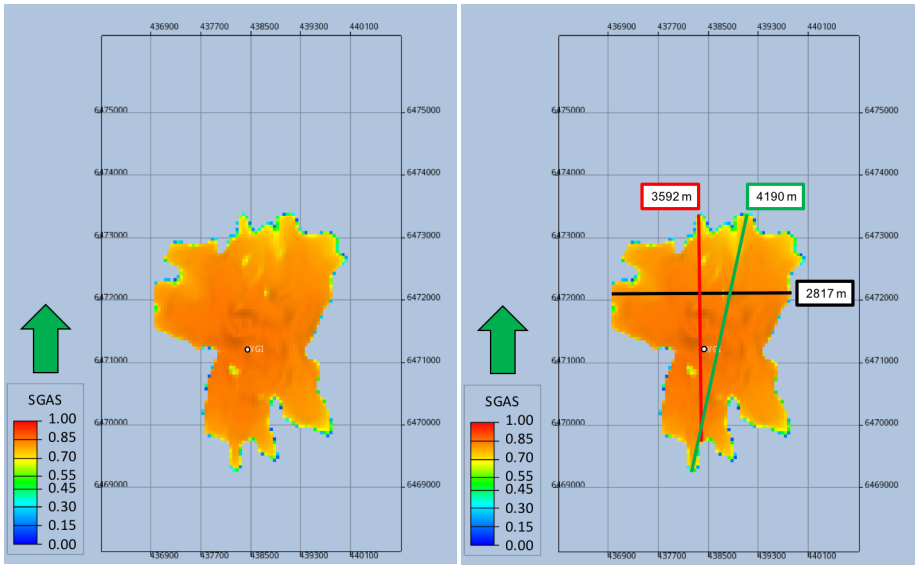

(a) Top plume geometry

(b) Top plume with measurements.

Figure 5.1: CASE 1: All sand, top plume geometry 1. October 2010.

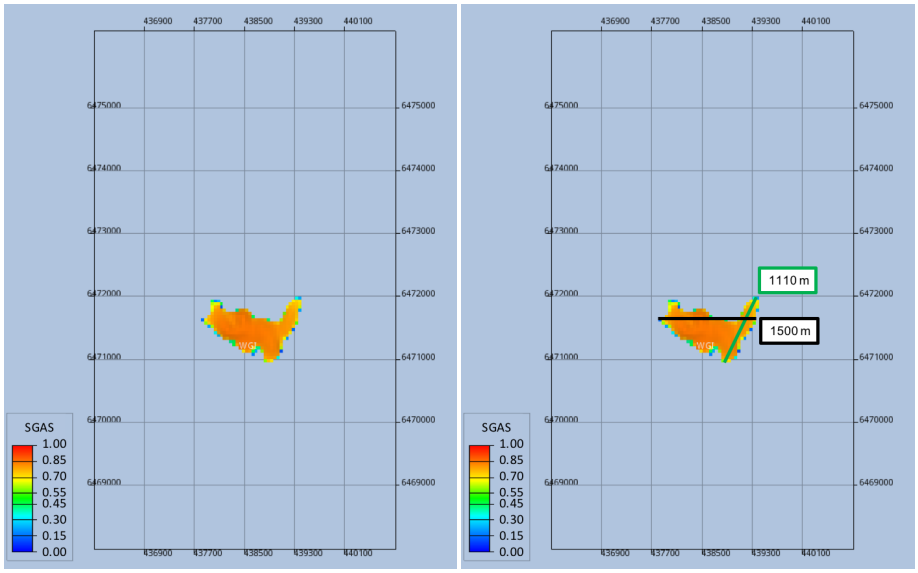

(a) Top plume without measurements **(b)** Top plume with measurements

Figure 5.2: CASE 2.1.1: Small MFC, top plume geometry 1. October 2010.

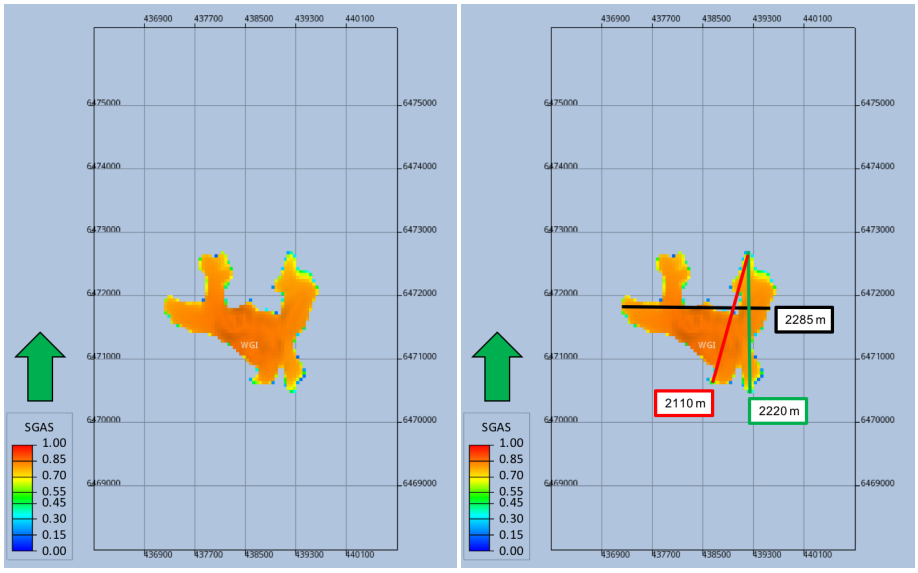

(a) The top plume with large MFC. **(b)** Top plume with measurements.

Figure 5.3: CASE 2.2.1: Large MFC, top plume geometry 1. October 2010.

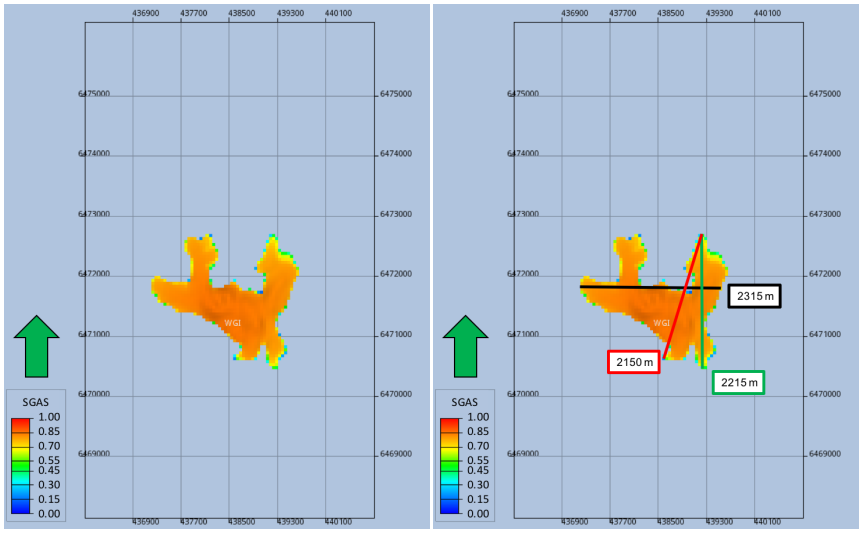

(a) Top plume geometry. **(b)** Top plume with measurements.

Figure 5.4: CASE 2.3.1: MFC, top plume geometry 1. October 2010.

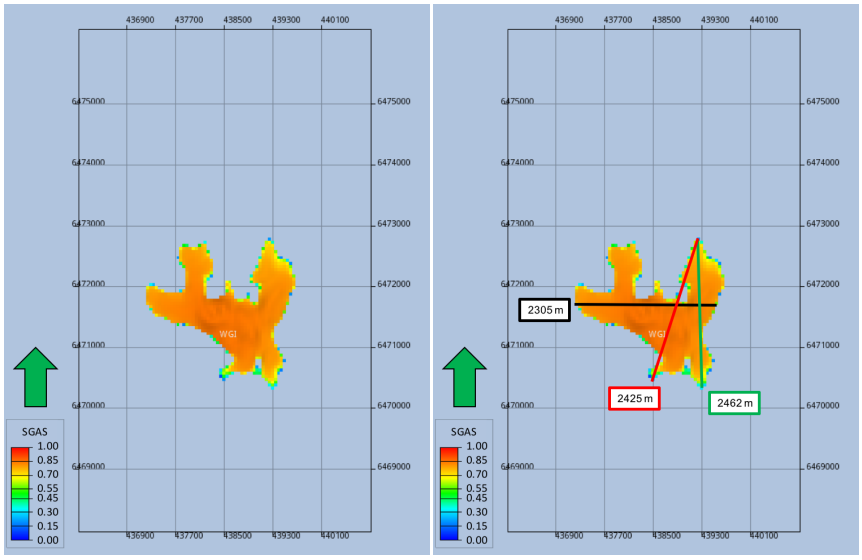

(a) Top plume geometry. **(b)** Top plume with measurements.

Figure 5.5: CASE 2.4 MFC with reduced permeability, October 2010.

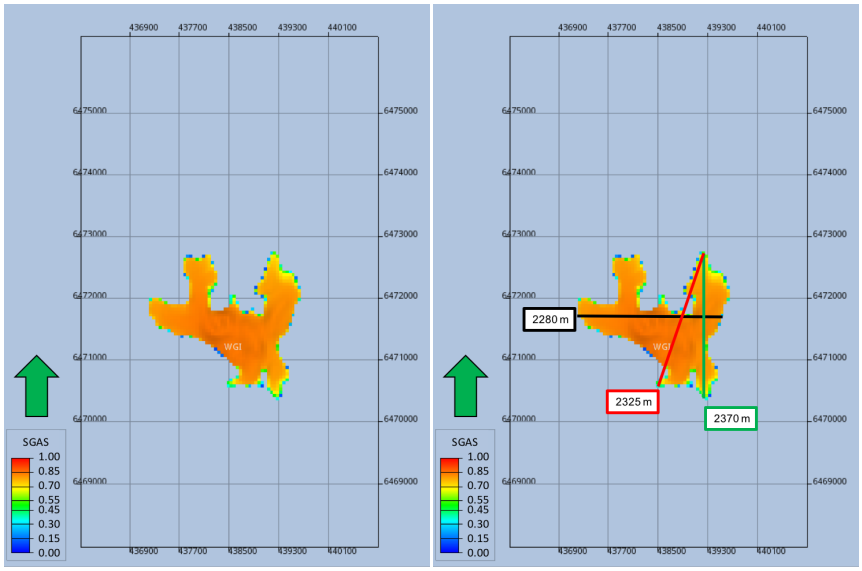

(a) Top plume geometry. **(b)** Top plume with measurements.

Figure 5.6: CASE 3.1 MFC with feeders, October 2010.

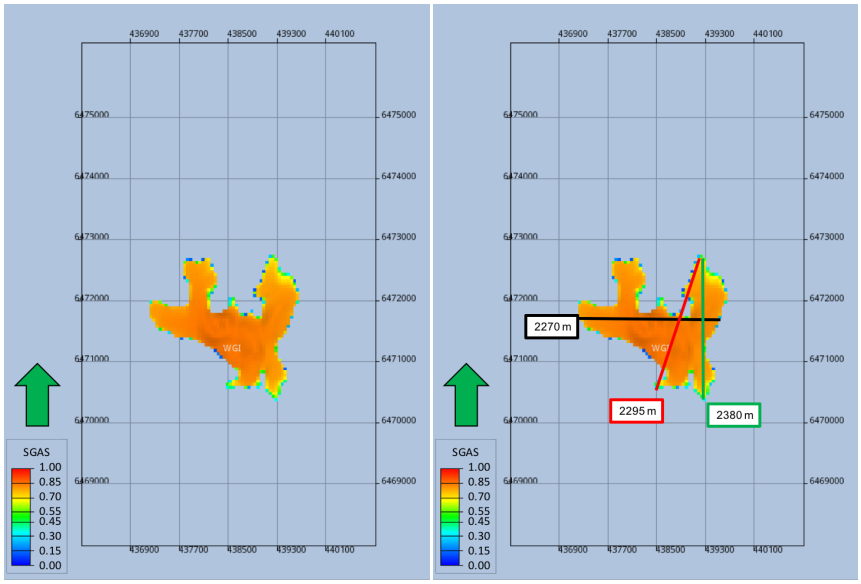

(a) Top plume October 2010. **(b)** Top plume with measurements.

Figure 5.7: CASE 3.2 MFC with feeders with reduced horizontal permeability.

5.1.8 Layering

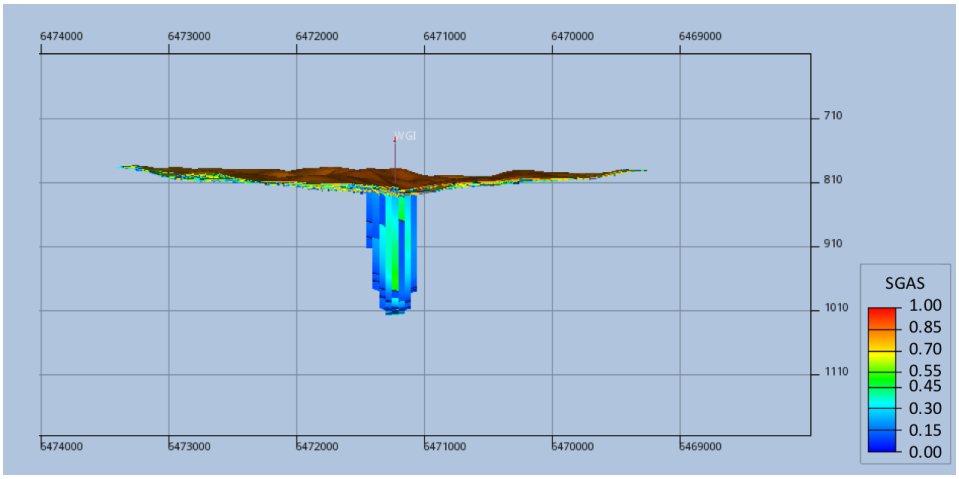

Figure 5.8: CASE 1: Plume 1. October 2010. Viewed from the East, with property filter 0.1-1 on gas saturation.

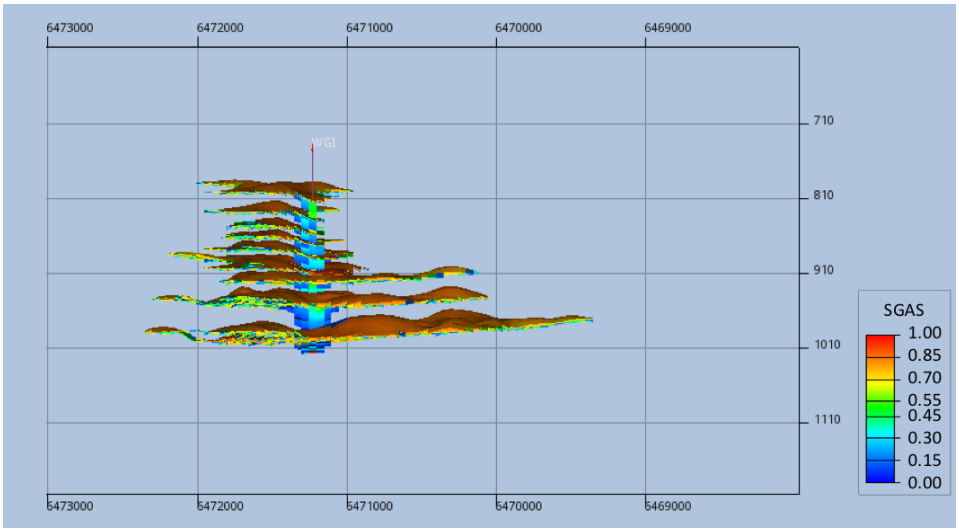

Figure 5.9: CASE 2.1.1: Small MFC, 1. October 2010, displayed from the East, and with a property filter excluding cells with <0.1 saturation of gas. It can be observed how the L1 layer is laterally extensive, and following layers decrease in size upward.

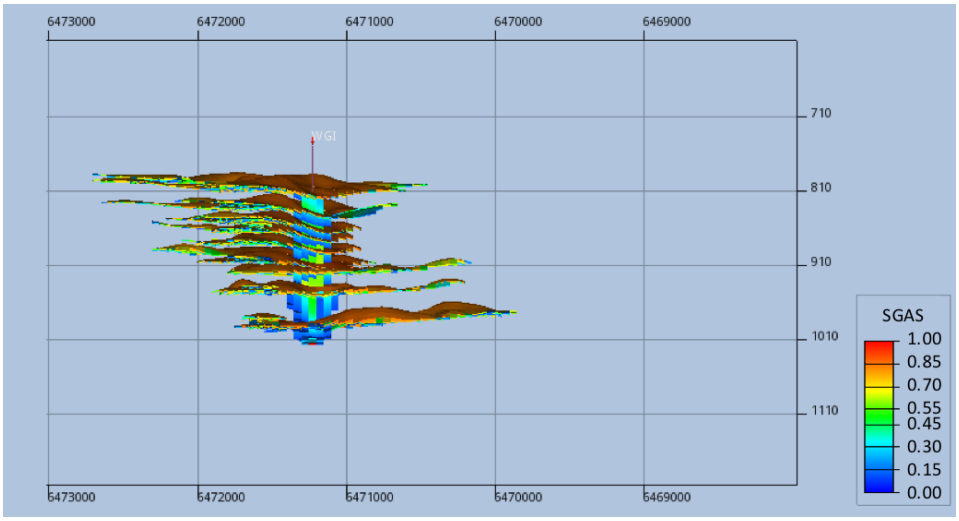

Figure 5.10: CASE 2.2.1: Large MFC, layering. With a bigger MFC the layers develop with more similar size, and the geometry of each layer develop according to the geometry of the corresponding intra-shale.

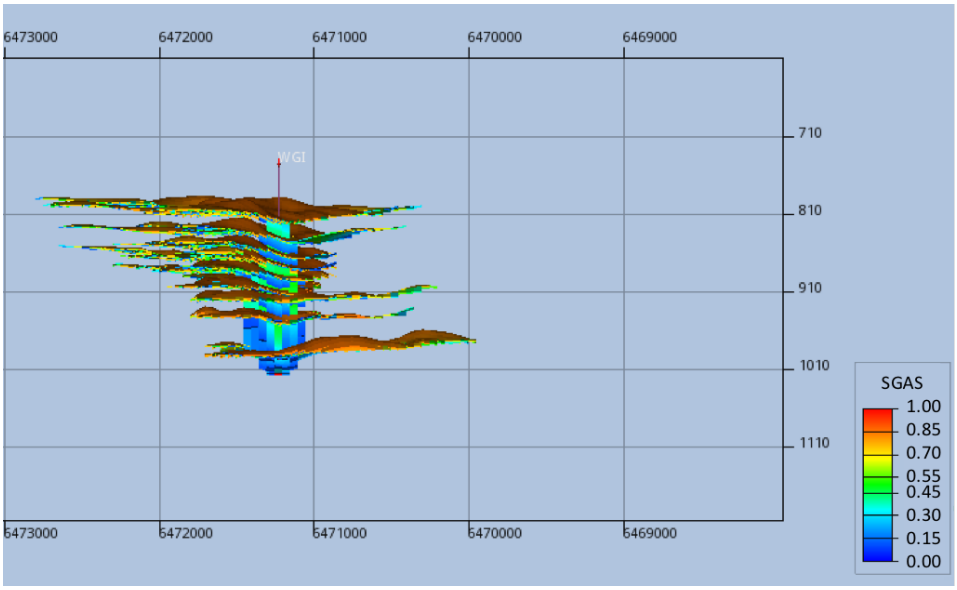

Figure 5.11: CASE 2.4: MFC with reduced horizontal permeability, more of the CO_2 gets distributed to the upper layers.

5.1.9 Top Arrival

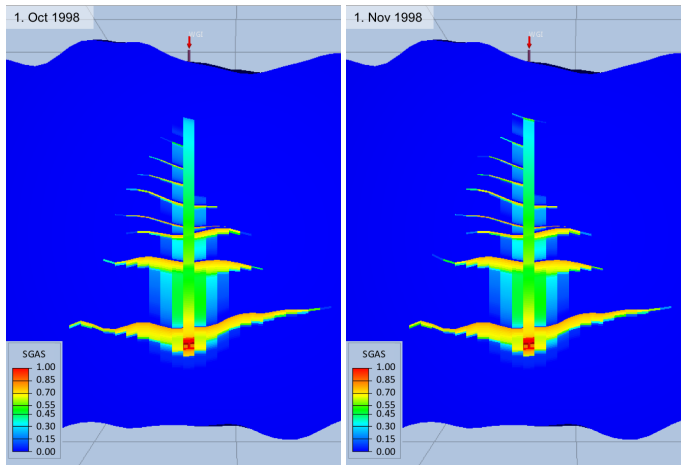

(a) **(b)**

Figure 5.12: CASE 2.1.1 The time frame where the CO_2 reaches the top of the reservoir. It is interpreted that the CO_2 reaches the top in October, and by November starts to laterally spread under the caprock.

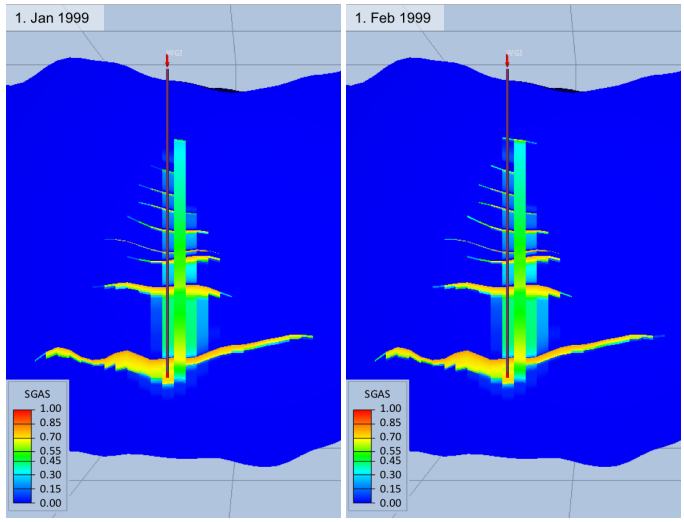

(a) **(b)**

Figure 5.13: CASE 2.1.2 The time frame where the CO_2 reaches the top of the reservoir. It is interpreted that the CO_2 reaches the top reservoir in January 1999, and start to spread laterally during January.

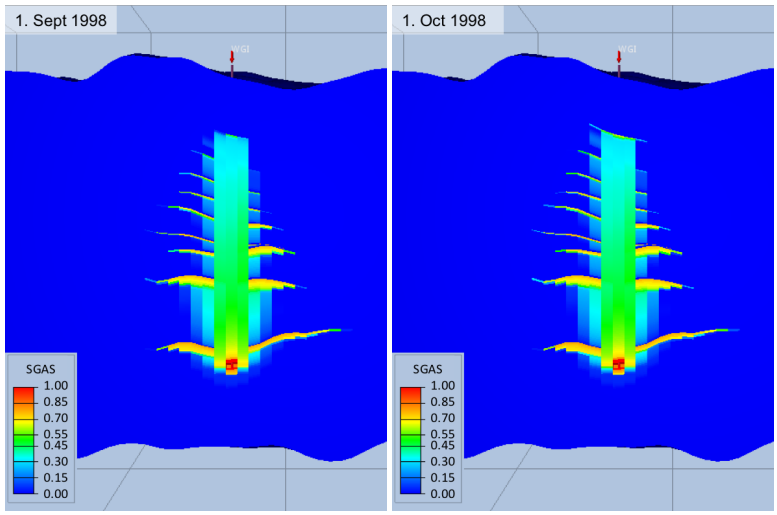

(a) **(b)**

Figure 5.14: CASE 2.2.1 The time frame where the CO_2 reaches the top of the reservoir. It is interpreted that the CO_2 reaches the top in October, and by November starts to laterally spread under the caprock.

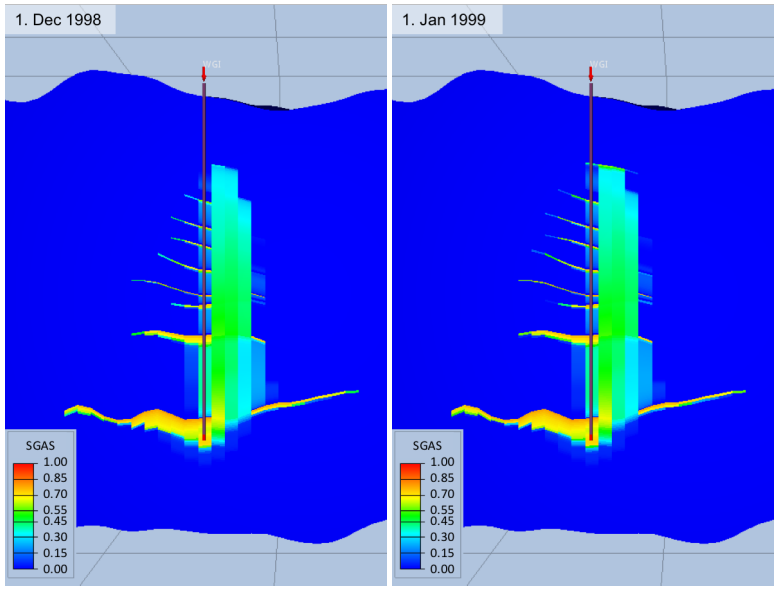

(a) **(b)**

Figure 5.15: CASE 2.2.2 The time frame where the CO_2 reaches the top of the reservoir. It is interpreted that the CO_2 reaches the top reservoir in December 1998, and start to spread laterally, resulting in a small layer accumulation 1. January 1999.

5.1.10 Feeders

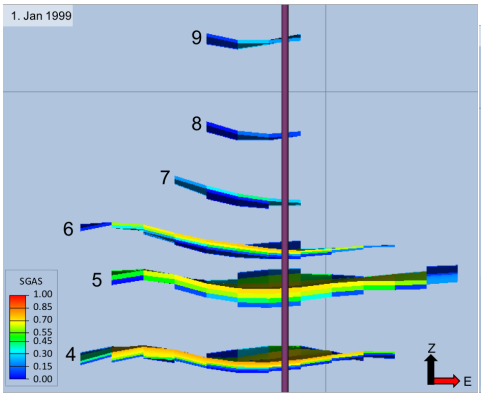

(a) 1. January 1999

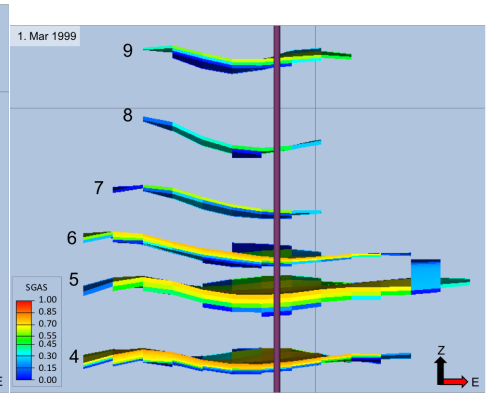

(b) 1. March 1999

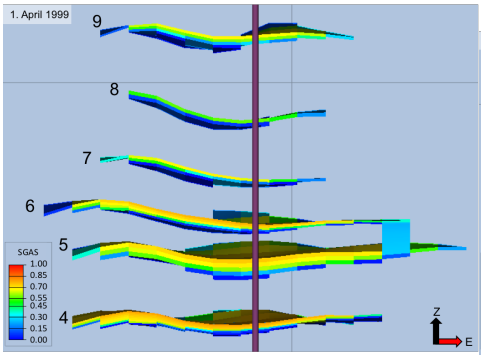

(c) 1. April 1999

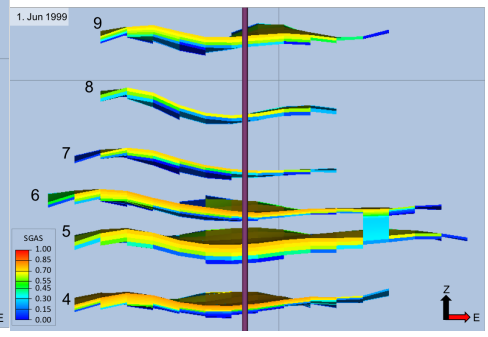

(d) 1. June 1999

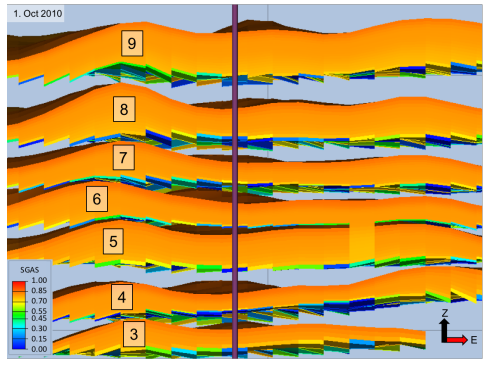

(e) 1. October 2010

Figure 5.16: CASE 3.1: MFC with Feeders. The NE1 Feeder.

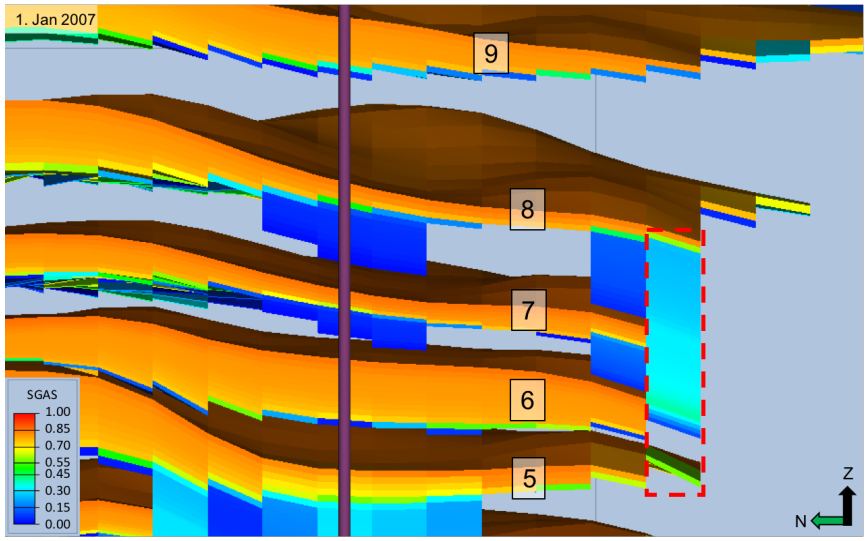

Figure 5.17: CASE 3.1: MFC with Feeders. At the time of placement, January 2007, of the SW1, the CO_2 in the overlying layer has already started to migrate into the feeder. Layer 5 however, has not expanded to that location.

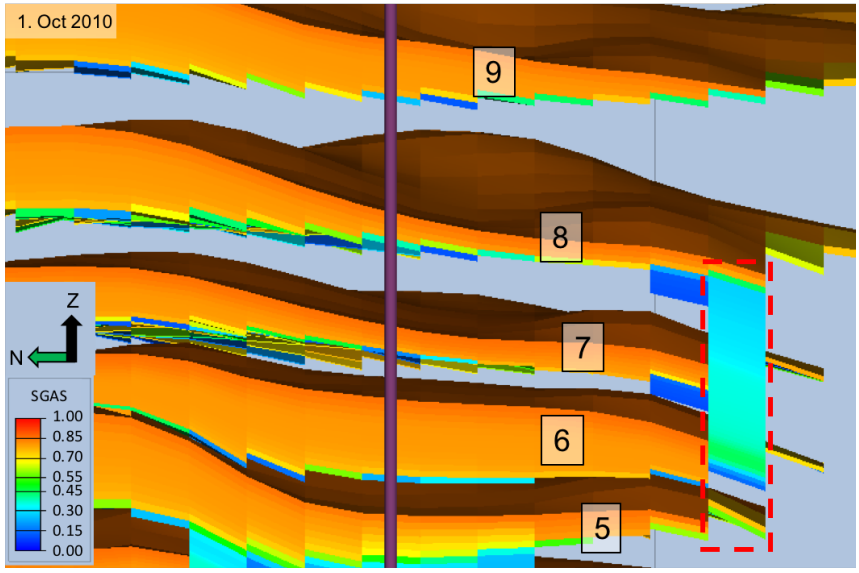

Figure 5.18: Case 3.2: MFC, feeders with reduced horizontal permeability. The SW1 feeder October 2010. Similar to the Case 3.1, the CO_2 does not reach this cell, and the feeder is sourced from Layer 6.

5.2 Seismic Interpretation

5.2.1 Data Quality: Phase and Polarity

There are two different polarity conventions used in the industry; American and European (or Australian) polarity. The American standard is that an increase in impedance results in positive amplitudes, normally displayed as red. European polarity gives negative amplitudes when there is an increase in impedance, shown as blue in the color display. Wavelet phase must also be determined. The most optimal for seismic interpretation is zero phase because it is easier and more intuitive to visualize as the maximum amplitude corresponds to the reflected interface (Herron, 2011).

The wavelet phase is estimated most accurately using deterministic methods using well control. Without well control one can visually estimate wavelet phase by observing certain reflections. No single boundary is foolproof, but the best horizons used to visually estimate the wavelet phase are the seafloor and hydrocarbon/water contact (seismic flat spot). Less reliable horizons are top of salt/volcanics, base of salt and basement reflectors, those should be used with care. Observing the seabed reflection, the seismic signal as it goes from water to sediment, is a secure way to find an increase in impedance. Using deterministic method of well control, correlating well information to reflection seismic data, and creating a link between time and depth domains. Synthetic seismogram is created from sonic and density logs from borehole evaluation program, in addition to check shots. There is always uncertainty in correlating well information to the seismic. The primary sources of uncertainty is; (1) the quality of the seismic data the well is being correlated to, and (2) assumptions made in generating the synthetic seismogram. More factors to consider if the well-to-seismic tie does not work are if the time-depth relationship is incorrect or if the logs used to generate the synthetic seismogram were not edited properly (Herron, 2011).

In this project the phase and polarity were decided by seabed observation. The seabed reflection, increase in impedance, in the 2010 dataset was red, establishing American polarity. Further, the wavelet looked to be zero phase, Figure 5.19. Same for the 1994 and 1999 datasets with 01 processing.

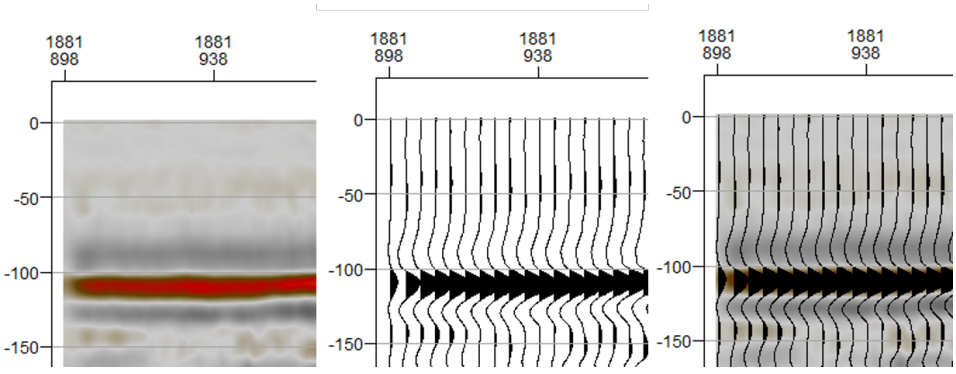

Figure 5.19: The seabed in the 2010 seismic, red indicating an increase in impedance at the seabed. Further the wavelet is zero phase.

5.2.2 Interpretation

Comparing the 1994 (baseline) and the 1999 seismic surveys, there were observed some shallow gas in both. In the 1999 survey the plume can clearly be observed as stacked amplitudes. Under the stacked amplitudes there is an gas wipe-out zone. In the Sand Wedge there is an small change in amplitude, the interpretation is that the CO_2 just arrived at this level. The layers of the plume have a similar lateral extent.

In the 2010 survey, Figure 5.21, the same shallow gas were observed, unchanged. The top layers are easily identified, but the lower layers are masked by gas wipe-out effect.

Top Plume Interpretation. The top plume was clearly defined on the seismic section, by a clear decrease in acoustic impedance, soft kick. The top plume interpreted has an elongated shape, measuring 1160m East-West, 2800m North-South and 3930 across, Figure 5.22.

5.3 Summary Table of Results

	Top Utsira Arrival	Top Plume measurements [NS, EW, across]
Seismic interpretation	1999	2800m, 1160m, 3930m
Base Case	-	-
Case 1	October 1998	3592m*, 2817m, 4190m
Case 2.1.1	October 1998	-, 1500m, 1110m
Case 2.1.2 (displaced)	January 1999	-
Case 2.2.1	September 1998	2220m, 2285m, 2110m
Case 2.2.2 (displaced)	December 1998	-
Case 2.3.1	September 1998	2215m, 2315m, 2150m
Case 2.3.2	September 1998	
Case 2.4	July 1998	2462m, 2305m, 2425m
Case 3.1	September 1998	2370m, 2280m, 2325m
Case 3.2	September 1998	2380m, 2270m, 2295m

Table 5.1: Summary table of some of the findings. *The North-South measurement for Case 1 was taken at a different location than the other cases due to different plume geometry, and the goal to capture the extent.

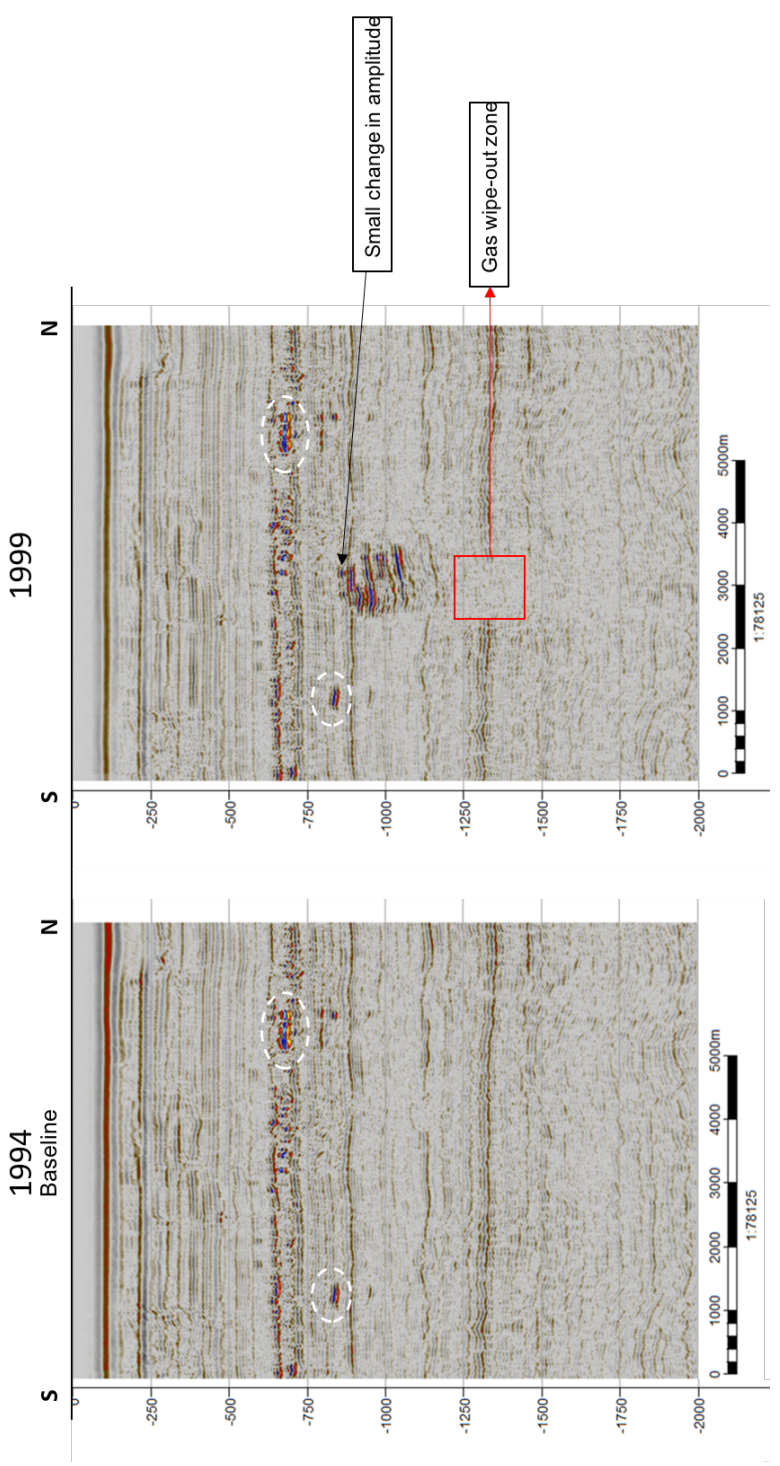

Figure 5.20: Inline 1844. Shallow gas in white circles. In the 1999 survey the plume can clearly be observed as stacked amplitudes. Under the stacked amplitudes there is an gas wipe-out zone. In the Sand Wedge there is an small change in amplitude, the interpretation is that the CO_2 just arrived at this level.

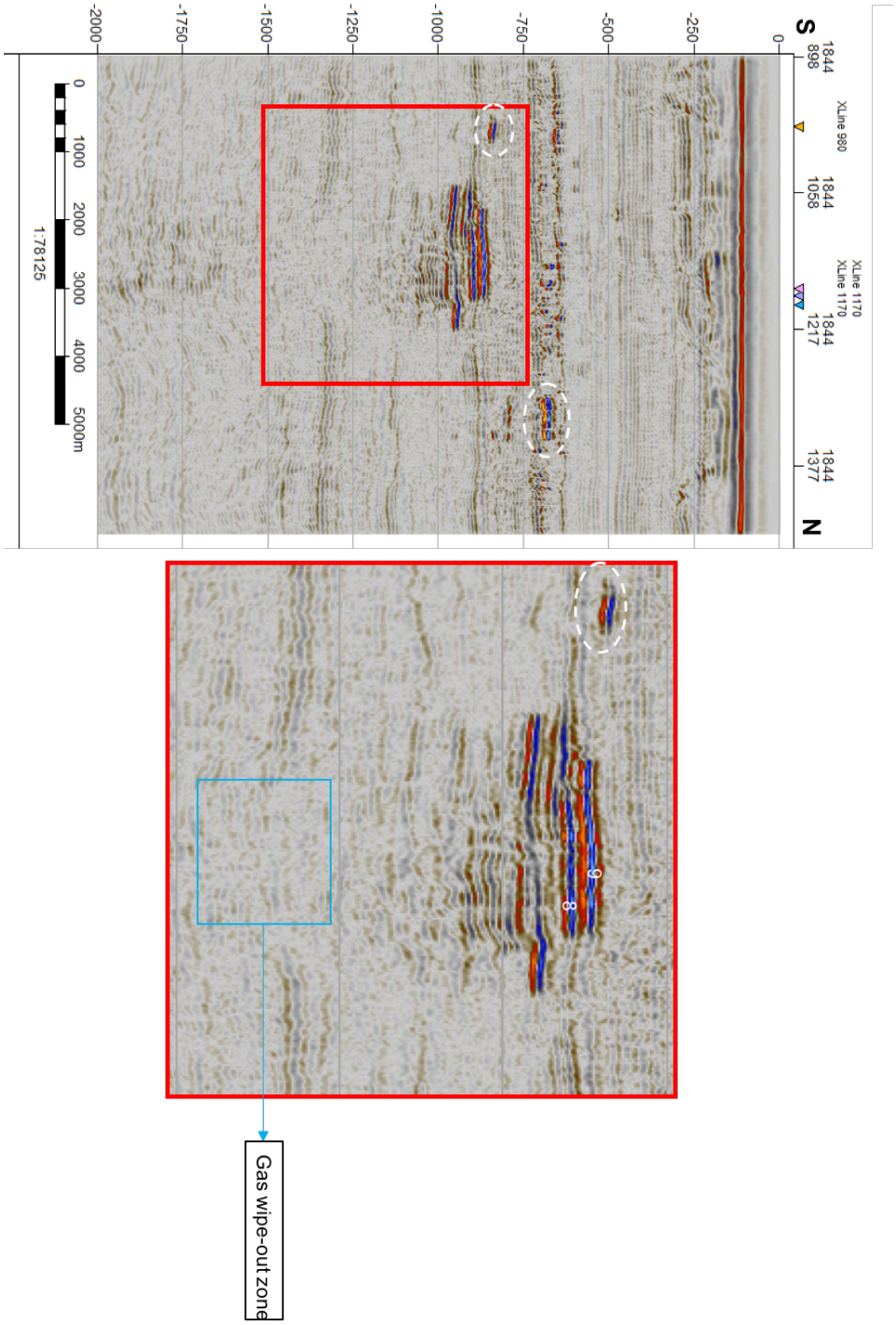

Figure 5.21: Inline 1844. The CO_2 plume in the 2010 survey, with gas wipe-out zone underneath. Top Layer 9 was easy to identify, similar to Layer 8.

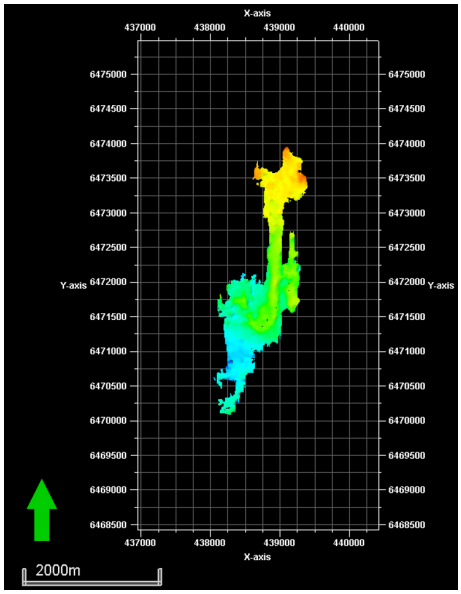

(a) The interpreted top plume from the 2010 seismic dataset.

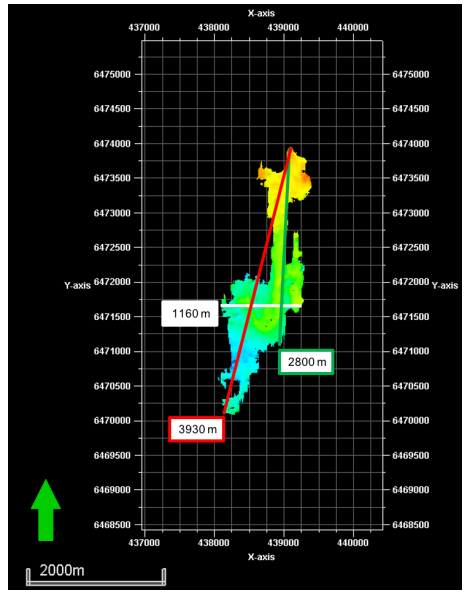

(b) The interpreted top plume from the 2010 seismic dataset with measurements taken in Petrel with measuring tool.

Figure 5.22: Top plume interpreted, 2010

Chapter 6

Discussion, Conclusions and Future Work

6.1 Discussion

The base case, where the CO_2 is contained under the lowermost shale, establish the sealing properties of the intra-reservoir shales. Further, the results from Case 1 establish that top arrival with no barriers in the reservoir would be October 1998.

The results from Case 2, the shale barriers help distribute the CO_2 laterally in the reservoir and create the layered plume even with just one main feeder. Comparing Case 2.1: MFC, Small and Case 2.2: MFC, Large, the smaller MFC results in a more laterally extensive distribution in Layer 1, while the bigger MFC create a more evenly distributed layers.

Furthermore, the size and placement of the MFC affect top arrival, and the shape of the top layer. The slightly displaced MFC results in later top arrival of the CO_2. From the seismic survey, acquired in early October 1999, it was interpreted that the CO_2 had just arrived at the top reservoir level. All the simulations with a MFC top arrival happens before October 1999. The earliest top arrival was the simulation with reduces horizontal permeability in the MFC, with top arrival already July 1998. It can be discussed that when the horizontal permeability is reduced, the CO_2 migrate vertically before laterally.

Case 3.1 and 3.2 with the feeders have the same top arrival time as the similar case without feeders, thus, the feeders do not influence the top arrival.

The top arrival is not affected by the size of the lower MFC. Nevertheless, this can also be explained by the placement of the MFC, because all of the cases with larger MFC at depth are placed so that there are no barrier to flow to the top.

The layers in each simulation develop with very similar geometry. From the seismic it is observed different lateral extent of the different layers. Suggesting that its possible the sand in Utsira do have some flow heterogeneties, and that uniform property used in these simulation does not capture that. Further, the MFC could have heterogeneties causing

different layering and slightly different placement of MFC can effect how the CO_2 migrate into each individual layer.

The top plume have a more rounded shape compared to the elongated shape from the seismic interpretation. This project focused on vertical flow features and kept the properties of the sand in the reservoir homogeneous, but these results suggest that there are more governing the shape and geometry of the CO_2 plume. It can be argued that this support the theory of more feeders than the ones already identified. Allowing a more lateral distribution of CO_2 and a more elongated top plume geometry. Further, the sand in the reservoir could be more heterogeneous, and inhabit more diverse flow properties, which also could contribute to more lateral distribution, and more elongated shape of the top plume.

Comparing the seismic interpretation with the Eclipse simulations; the EW width of the top plume is most similar to Case 2.1.1: small MFC, placed directly over the injection point. However, the Case 2.1.1 does have a smaller measurement across than what is observed in seismic, and not the same geometry as the simulation does not include the northward migration. In the modelling results the Layer 1 consistently migrated to an anticlinal structure South of the injection point, extending further to the South than any other layer. The overlying layers had a more inclination of migrating into anticlinal structures to the North of the MFC. Still, in the seismic interpretation Layer 1 is not extending toward the South.

6.2 Conclusions

The interpretation of the depositional environment of the Utsira Fm ranges from shallow marine/deltaic (Ramberg et al., 2013), inner shelf in the Completion Report to low-stand fan (Chadwick et al., 2004b).

From literature authors have proposed a number of different explanations for the fast ascend of the injected CO_2. One can categorize these into two categories; geological and non-geological explanations. The geological explanations can be summarized as low threshold pressures (Cavanagh and Haszeldine (2014)), discontinuous shale layers (Furre et al. (2017), Lindeberg et al. (2000), Cavanagh and Haszeldine (2014)), micro-fractures from eg. ice sheet unloading (Cavanagh and Haszeldine, 2014), and sand injectites (Zweigel et al., 2004). On the other hand, non-geological factors proposed are CO_2 dehydration of shales (Chadwick et al. (2004a)) and mechanical force of the (Chadwick et al. (2004a)).

The base case, sand reservoir with intra-shale barriers, the modelling resulted in the CO_2 not surpassing the lowest intra-shale barrier between Layer 1 and Layer 2. The CO_2 was contained in Layer 1, and accumulated under the intra-shale following the geometry of the shale, according to spill-point analysis. From this it can be concluded that some form of migration pathway through the shale barriers is present allowing the CO_2 to migrate to the top reservoir, as interpreted from the seismic surveys conducted.

None of the modelled top layer geometries match the seismic interpretation, the results from the simulations are too wide compared to the seismic. The simulation with closest East-West width is Case 2.1.1 with small MFC. However, the NS extent of the plume interpreted from seismic is closer to the cases with large and increasing in size MFC,

and the across measurement is closest to case 1, with only sand in the reservoir. On the other side, Case 1 with only sand in the reservoir have a different geometry, best described as elliptical, while the interpreted top plume has this elongated shape. From this it can be concluded that none of the cases investigated capture everything happening in the reservoir, and further research is needed for more understanding of the geological structures in the reservoir and subsequently the resulting flow effects.

Finally, from the modelling results it is reasonable to conclude that the Utsira Fm contain intra-reservoir barriers with zones of higher permeability, allowing the CO_2 to move vertically in the reservoir. Further, it can be concluded that the intra-shale help distribute the CO_2 horizontally in the reservoir, creating a layered plume, but also govern size and shape of the top layer.

6.3 Future Work

- In this work the focus was the already identified feeders and their implications on fluid flow in the storage reservoir. Based on the results and the conclusion in this work that more migration pathways are present to produce the observed top plume in the seismic. The next step would be to include more feeders.
- Due to time constraints the feeders were applied to only one case of MFC. Applying the feeders to more cases of MFC would potentially further improve the understanding of the feeders.
- The flow effects of sand injectites are investigated, but due to limited studies of the porosity and permeability characteristics of sand injectites the representation of those features are a best-guess. To attain a better understanding of the flow effects the sand injectites properties need to be refined.
- The geological scenarios applied in here have all sand as a main lithology, and thus, also sand properties. To get a better understanding of the geological features creating scenarios with more heterogeneity could be beneficial.
- The main focus of this thesis has been to improve the geological interpretation of the intra-shale barriers based on Eclipse 300 modelling and fluid flow within the reservoir. Thus, the simulation is stopped at shut-in. To understand the long term fluid behaviour in the reservoir, and thus, conformance monitoring, continue the simulation into the future.
- The modelling in this work is preformed without capillary pressure. The initial plan to preform modelling with capillary pressure was disregarded due to time constraints, and the COVID-19 situation. Modelling with capillary pressure and entry pressure of the shales, one would get an even better understanding of the subsurface flow dynamics and the effects of the feeders.

Bibliography

Ahr, W.M., 2008. Geology of Carbonate Reservoirs: The Identification, Description and Characterization of Hydrocarbon Reservoirs in Carbonate Rocks. 3 ed., WILEY. An optional note.

Baklid, A., Korbol, R., Owren, G., 1996. Sleipner vest co2 disposal, co2 injection into a shallow under- ground aquifer, SPE paper 36600-MS presented at SPE Annual Technical Conference and Exhibition.

Brown, A.R., 2011. Interpretation of Three-Dimensional Seismic Data. The American Assosiation of Petroleum Geologists and the Society of Exploration Geophysics.

Burnside, N., Naylor, M., 2014. Review and implications of relative permeability of co2/brine systems and residual trapping of co2. International Journal of Greenhouse Gas Control 23, 1–11. doi:10.1016/j.ijggc.2014.01.013.

Cavanagh, A., Haszeldine, R., 2014. The sleipner storage site: Capillary flow modeling of a layered co2 plume requires fractured shale barriers within the utsira formation. International Journal of Greenhouse Gas Control 21, 101–112. doi:http://dx.doi.org/10.1016/j.ijggc.2013.11.017.

Chadwick, A., Eiken, O., 2013. Chapter 10: Offshore co2 storage: Sleipner natural gas field beneath the north sea .

Chadwick, R., Arts, R., Eiken, O., Kirby, G., Lindeberg, E., Zweigel, P., 2004a. 4d seismic imaging of an injected co2 plume at the sleipner field, central north sea. Geological Society London Memoirs 29, 311–320. doi:10.1144/GSL.MEM.2004.029.01.29.

Chadwick, R., Zweigel, P., Gregersen, U., Kirby, G., Holloway, S., Johannessen, P., 2004b. Geological reservoir characterisation of co2 storage site: The utsira sand, sleipner, nothern north sea. Energy , 1371 – 1381doi:10.1016/j.energy.2004.03.071.

Completion Report, . Completion report well 15/9-13. URL: https://factpages.npd.no/pbl/wellbore_documents/45_15_9_13_Completion_report_and_log.pdf.

Eiken, O., Ringrose, P., Hermanrud, C., Nazarian, B., Torp, T.A., Høier, L., 2011. Lessons learned from 14 years of ccs operations: Sleipner, in salah and snøhvit. Energy Procedia 4, 5541–8. doi:https://doi.org/10.1016/j.egypro.2011.02.541.

Encyclopaedia Britannica, . Carbon dioxide. URL: https://www.britannica.com/science/carbon-dioxide.

Equinor, a. Sleipner 2019 benchmark model. doi:10.11582/2020.00004.

Equinor, b. Sleipner 4d seismic dataset. doi:10.11582/2020.00005.

Furre, A., Ringrose, P., Santi, A., 2019. Observing the invisible - co2 feeder chimneys on seismic time-lapse data .

Furre, A.K., Eiken, O., Alnes, H., Vevatne, J.N., Kiær, A.F., 2017. 20 years of monitoring co2-injection at sleipner. Energy Procedia 114, 3916–3926. doi:https://doi.org/10.1016/j.egypro.2017.03.1523.

Fyfe, J.A., Gregersen, U., Jordt, H., Rundberg, Y., Eidvin, T., Evans, D., Stewart, D., Hovland, M., Andresen, P., 2003. The Millennium Atlas: petroleum geology of the central and northern North Sea. London: The Geological Society of London.

Ganesh, P.R., Bryant, S.L., Meckel, T.A., 2013. Characterizing small-scale migration behavior of sequestered co2 in a realistic geologic fabric. Energy Procedia 37, 5258–5266. doi:10.1016/j.egypro.2013.06.442.

Halland, E.K., Gjeldvik, I.T., Johansen, W.T., Magnus, C., Meling, I.M., Pedersen, S., Riis, F., Solbakk, T., Tappel, I., 2019. CO2 Storage Atlas, Norwegian Continential Shelf, Ch. 4. The Norwegian North Sea. NPD.

Herron, D.A., 2011. First Steps in Seismic Interpretation. Society of Exploration Geophysicists.

Hurst, A., Scott, A., Vigorito, M., 2011. Physical characteristics of sand injectites. Earth-Science Reviews 106, 215–246. doi:https://doi.org/10.1016/j.earscirev.2011.02.004.

Krevor, S., J.Blunt, M., M.Benson, S., Pentland, C.H., Reynolds, C., Al-Menhali, A., Niu, B., 2015. Capillary trapping for geologic carbon dioxide storage – from pore scale physics to field scale implications. International Journal of Greenhouse Gas Control 40, 221–237. doi:https://doi.org/10.1016/j.ijggc.2015.04.006.

Lindeberg, E., Zweigel, P., Bergmo, P., Ghaderi, A., Lothe, A., 2000. Prediction of co2 distribution pattern improved by geology and reservoir simulation and verified by time lapse seismic, Cairns, Australia. Available at https://www.sintef.no/globalassets/project/ik23430000-sacs/publications/lindeberg_et_al_ghgt5.pdf/.

Nichols, G., 2009. Sedimentology and Stratigraphy. 2 ed., Wiley-Blackwell.

Nicoll, G.D., 2011. Evaluation of the Nordland Group overburden as an effective seal for the Sleipner CO2 storage site (offshore Norway) using analytical and stochastic modelling techniques. Ph.D. thesis. School of Geosciences, University of Edinburgh.

Parka, J., Fawada, M., Vikena, I., Akera, E., Bjørnaråa, T.I., 2013. Csem sensitivity study for sleipner co2-injection monitoring. Energy Procedia 37, 4199 – 4206. doi:10.1016/j.egypro.2013.06.322.

Ramberg, I.B., Bryhni, I., Nøttvedt, A., Rangnes, K., 2013. Landet Blir Til, Norges Geologi. Norsk Geologisk Forening.

Ringrose, P., Bentley, M., 2015. Reservoir Model Design, A Practitioner's Guide. Springer. doi:10.1007/978-94-007-5497-3.

Solomon, S., 2007. Carbon dioxide storage: Geological security and environmental issues – case study on the sleipner gas field in norway summary .

Thomas, L.K., Katz, D.L., Tek, M.R., 1968. Threshold pressure phenomena in porous media. Society of Petroleum Engineers 8. doi:10.2118/1816-PA.

White, J.C., Williams, G., Chadwick, A., Furre, A.K., Kiær, A., 2018. Sleipner: The ongoing challenge to determine the thickness of a thin co2 layer. International Journal of Greenhouse Gas Control 69, 81–95. doi:https://doi.org/10.1016/j.ijggc.2017.10.006.

Witkowski, A., Majkut, M., Rulik, S., 2014. Analysis of pipeline transportation systems for carbon dioxide sequestration. Archives of Thermodynamics 35, s. 117–140. doi:10.2478/aoter-2014-0008.

Zweigel, P., Arts, R., Lothe, A., Lindeberg, E., 2004. Reservoir geology of the utsira formation at the first industrial-scale underground co2 storage site (sleipner area, north sea). Geological Storage of Carbon Dioxide. Geological Society, London, Special Publications 233, 165–180. doi:http://dx.doi.org/10.1144/GSL.SP.2004.233.01.11.

Appendix A

A.1 Injection rate

The initial injection rate in one injection well is 19,000 tonnes/day CO2 (10 million sm3/day, 1 tonnes of CO2 is equal 517.6 Sm3), while the recent injection rate at Sleipner is approximately 2750 tonnes/day (1 Mt/year) (Eiken et al., 2011).

From paper; recent injection rate is 2750 tonnes/day (1Mt/year).

$$2750\frac{tonnes}{day}517.6\frac{Sm^3}{ton} = 1423400\frac{Sm^3}{day} \tag{A.1}$$

$$2750\frac{tonnes}{day}365\frac{days}{year} = 1003750\frac{tonnes}{year} \approx 1\frac{Mtonnes}{year} \tag{A.2}$$

A.2 Base Case Development

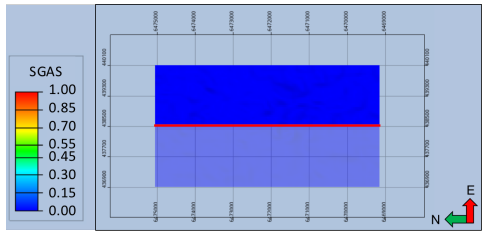

(a) Legend of gas saturation and orientation of cross section. Cross section marked by red line, and viewed from the East.

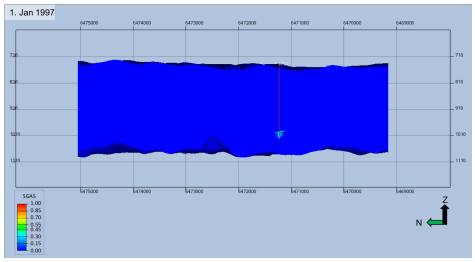

(b) Development 1. Jan 1997

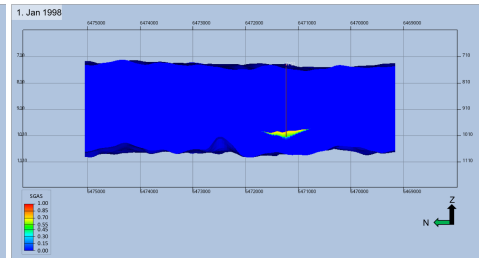

(c) Development 1. Jan 1998

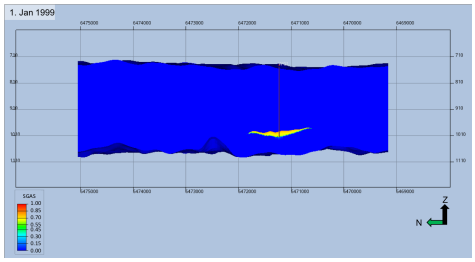

(d) Development 1. Jan 1999

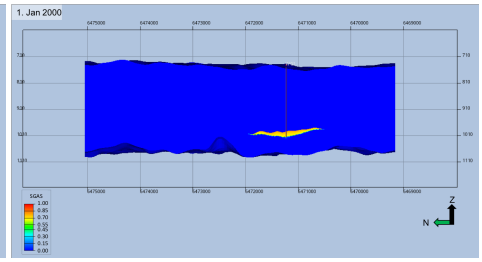

(e) Development 1. Jan 2000

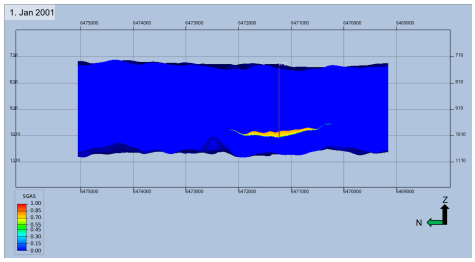

(f) Development 1. Jan 2001

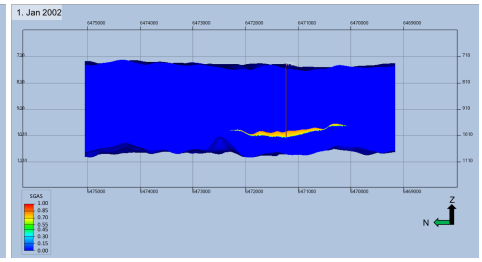

(g) Development 1. Jan 2002

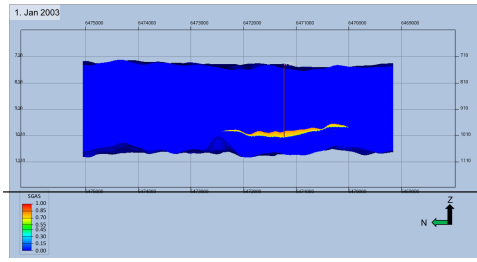

(h) Development 1. Jan 2003

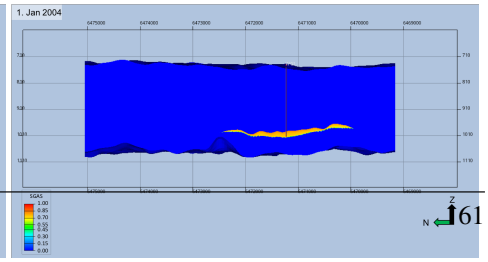

(i) Development 1. Jan 2004

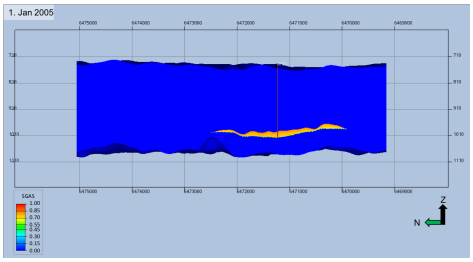

(j) Development 1. Jan 2005

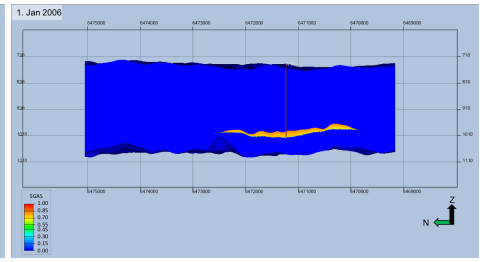

(k) Development 1. Jan 2006

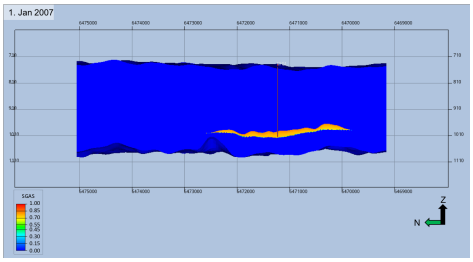

(l) Development 1. Jan 2007

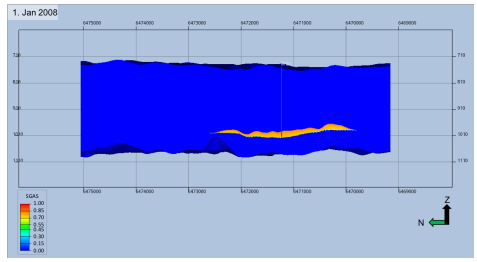

(m) Development 1. Jan 2008

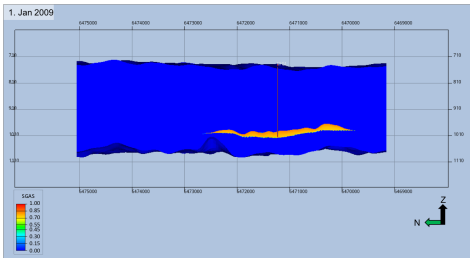

(n) Development 1. Jan 2009

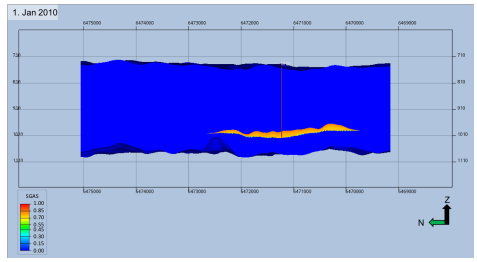

(o) Development 1. Jan 2010

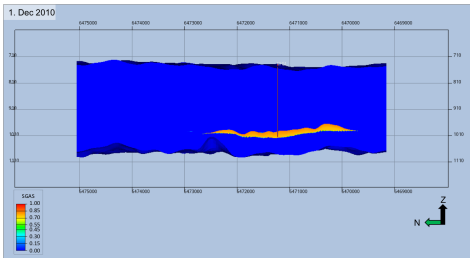

(p) Development 1. Dec 2010

Figure A.1: Plume development of the base case simulation. Visualized in ResInsight. Model viewed from the East. Cells with gas saturation. Viewed with a range filter, the cells 34-64.

A.3 Case 1 Development

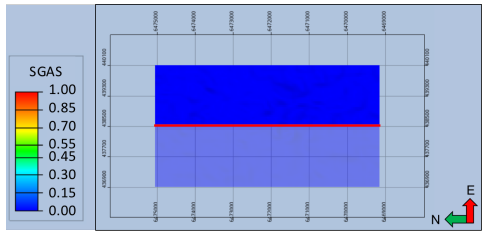

(a) Legend of gas saturation and orientation of cross section. Cross section marked by red line, and viewed from the East.

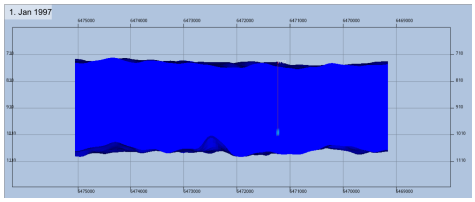

(b) Development 1. Jan 1997

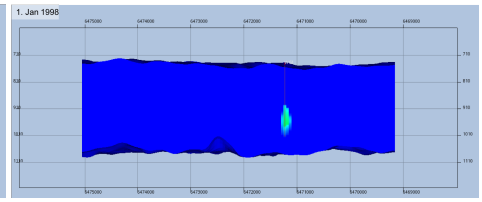

(c) Development 1. Jan 1998

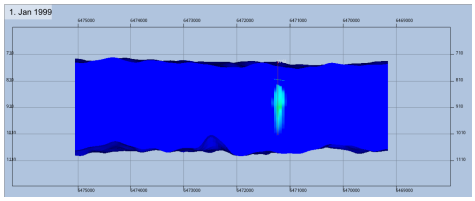

(d) Development 1. Jan 1999

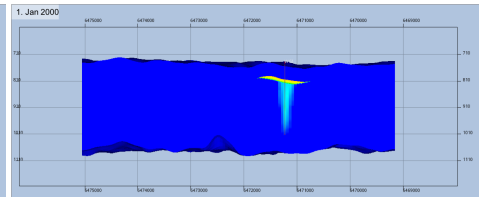

(e) Development 1. Jan 2000

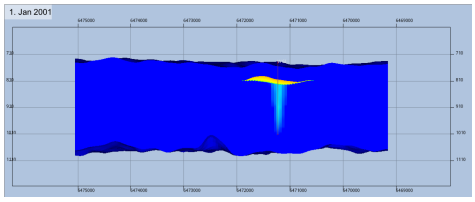

(f) Development 1. Jan 2001

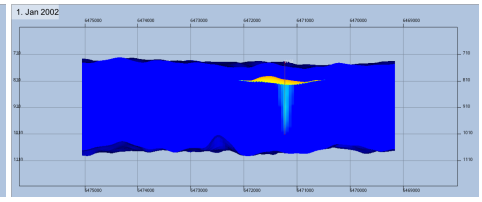

(g) Development 1. Jan 2002

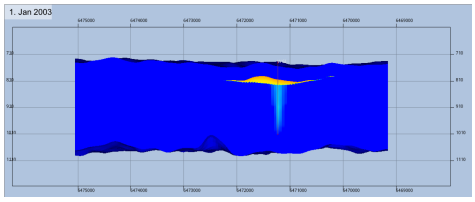

(h) Development 1. Jan 2003

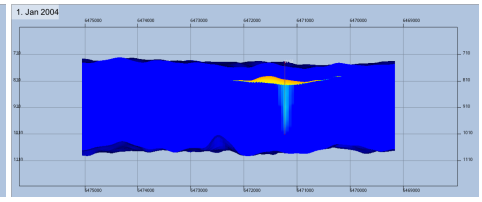

(i) Development 1. Jan 2004

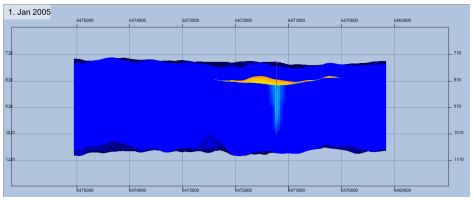

(j) Development 1. Jan 2005

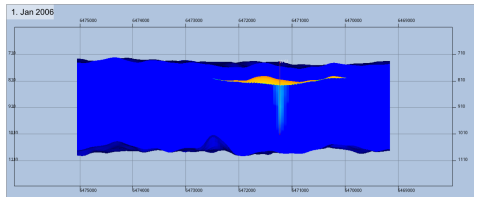

(k) Development 1. Jan 2006

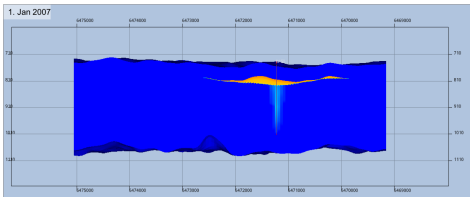

(l) Development 1. Jan 2007

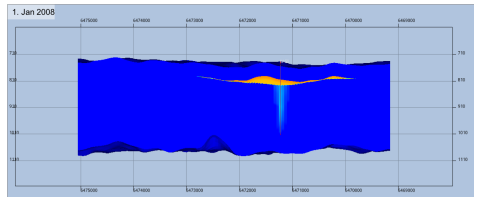

(m) Development 1. Jan 2008

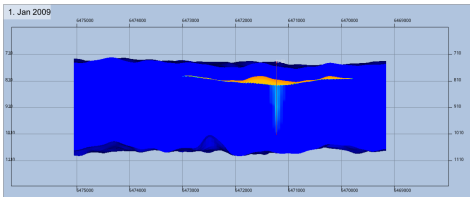

(n) Development 1. Jan 2009

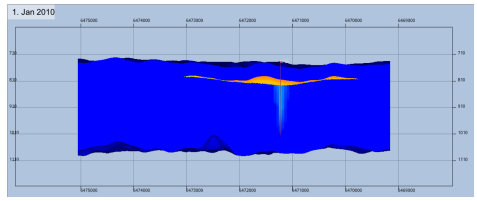

(o) Development 1. Jan 2010

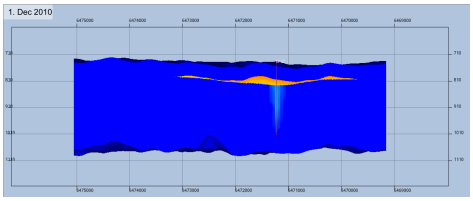

(p) Development 1. Dec 2010

Figure A.2: Plume development of the Case 1 simulation. Visualized in ResInsight. Model viewed from the East. Cells with gas saturation. Viewed with a range filter, the cells 34-64.

A.4 Case 2.1 Development

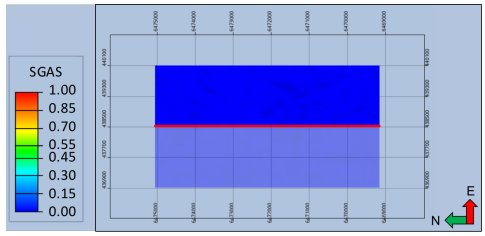

(a) Legend of gas saturation and orientation of cross section.
Cross section marked by red line, and viewed from the East.

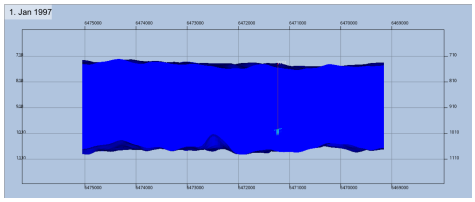

(b) Development 1. Jan 1997

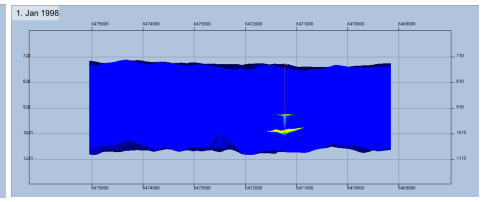

(c) Development 1. Jan 1998

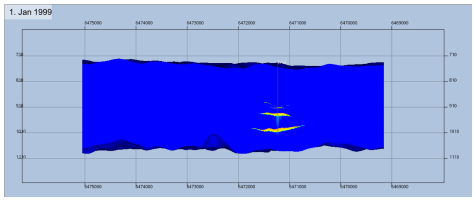

(d) Development 1. Jan 1999

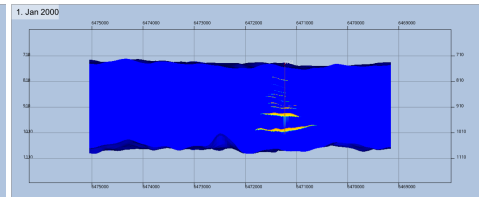

(e) Development 1. Jan 2000

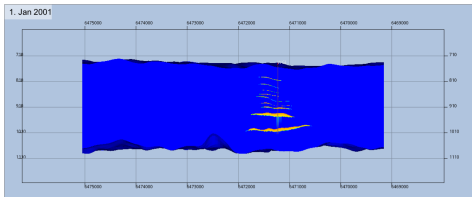

(f) Development 1. Jan 2001

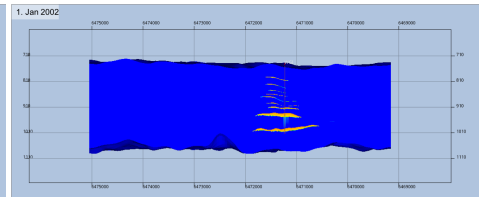

(g) Development 1. Jan 2002

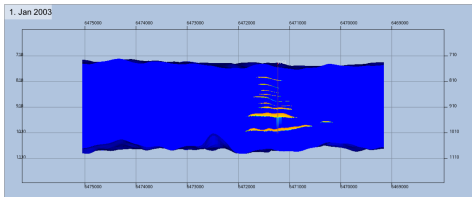

(h) Development 1. Jan 2003

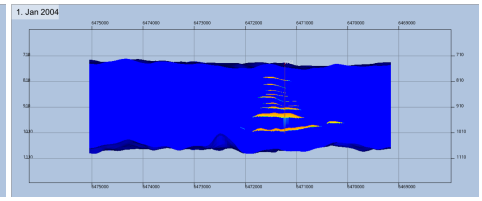

(i) Development 1. Jan 2004

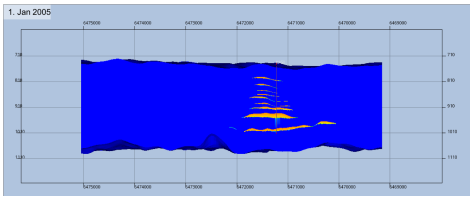

(j) Development 1. Jan 2005

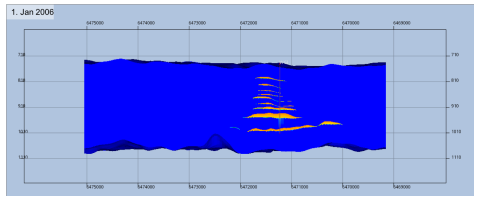

(k) Development 1. Jan 2006

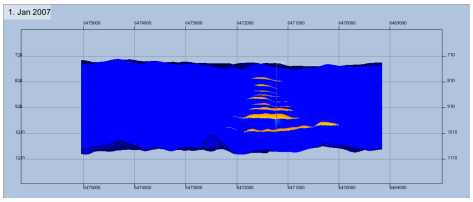

(l) Development 1. Jan 2007

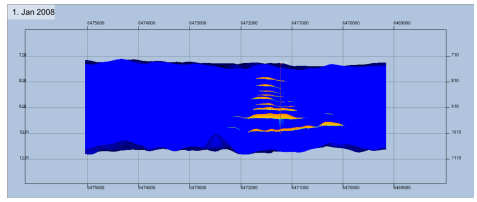

(m) Development 1. Jan 2008

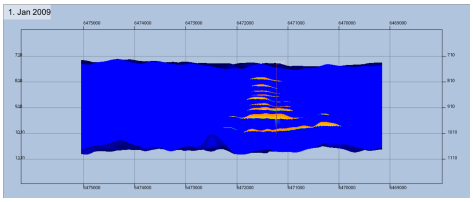

(n) Development 1. Jan 2009

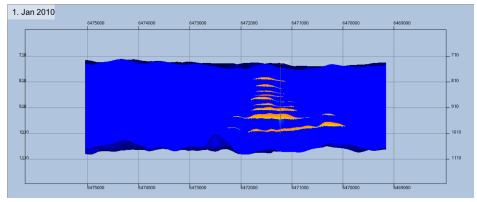

(o) Development 1. Jan 2010

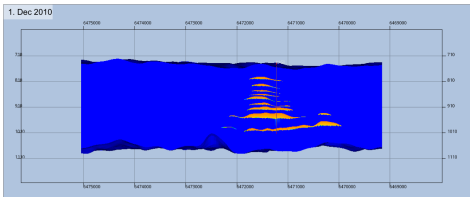

(p) Development 1. Dec 2010

Figure A.3: Plume development of the Case 2.1.1 simulation. Visualized in ResInsight. Model viewed from the East. Cells with gas saturation. Viewed with a range filter, the cells 34-64.

A.5 Case 2.2 Development

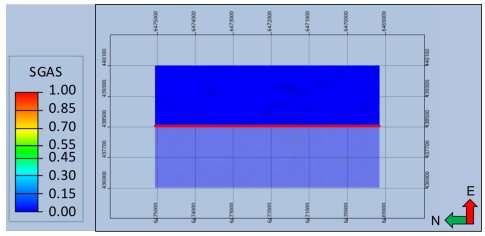

(a) Legend of gas saturation and orientation of cross section.
Cross section marked by red line, and viewed from the East.

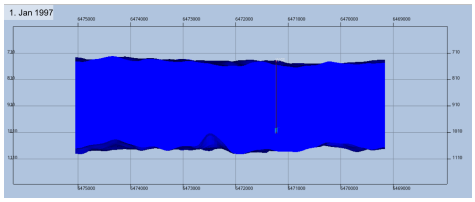

(b) Development 1. Jan 1997

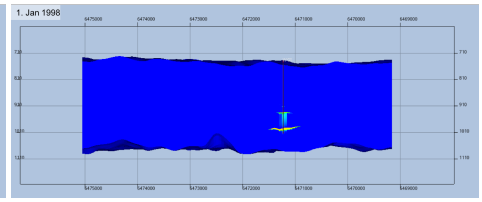

(c) Development 1. Jan 1998

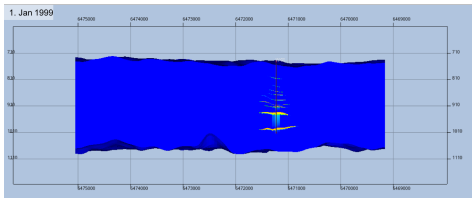

(d) Development 1. Jan 1999

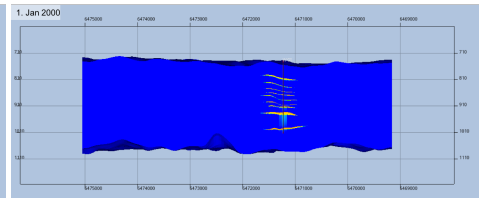

(e) Development 1. Jan 2000

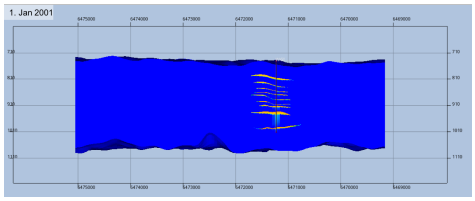

(f) Development 1. Jan 2001

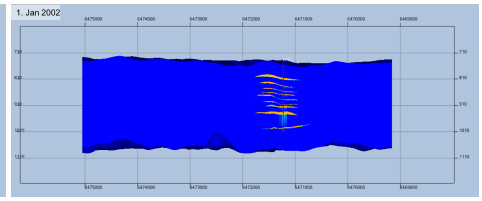

(g) Development 1. Jan 2002

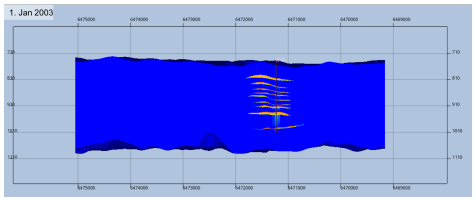

(h) Development 1. Jan 2003

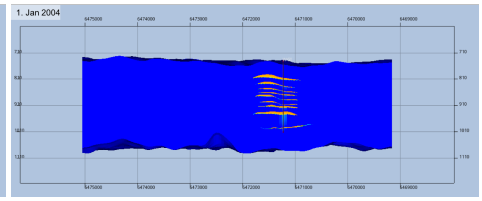

(i) Development 1. Jan 2004

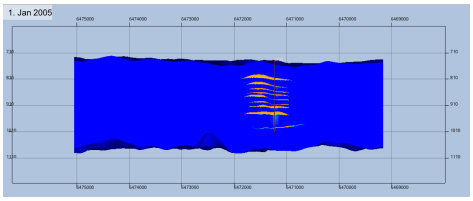

(j) Development 1. Jan 2005

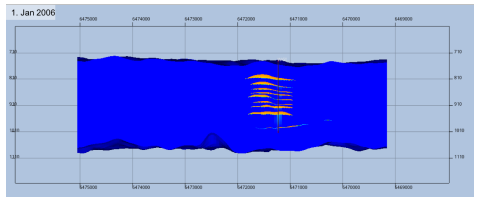

(k) Development 1. Jan 2006

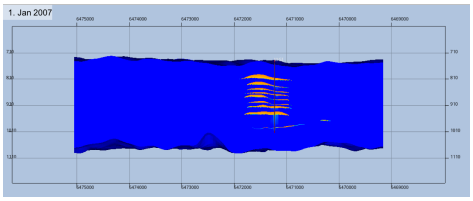

(l) Development 1. Jan 2007

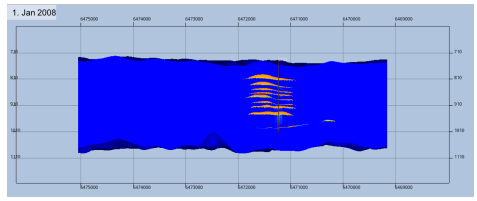

(m) Development 1. Jan 2008

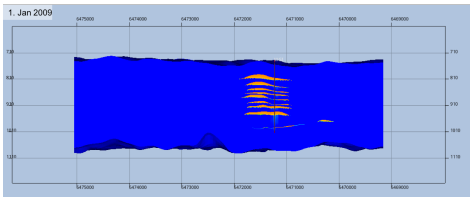

(n) Development 1. Jan 2009

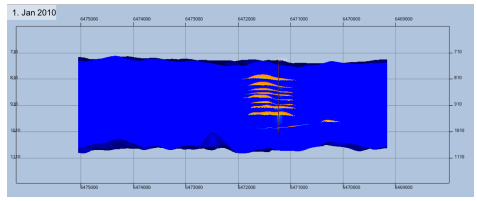

(o) Development 1. Jan 2010

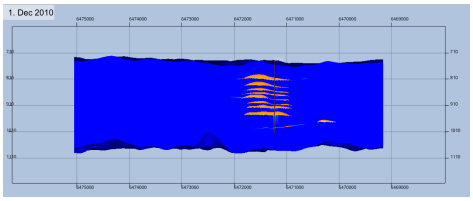

(p) Development 1. Dec 2010

Figure A.4: Plume development of the Case 2.2.1 simulation. Visualized in ResInsight. Model viewed from the East. Cells with gas saturation. Viewed with a range filter, the cells 34-64.

A.6 Case 2.4 Development

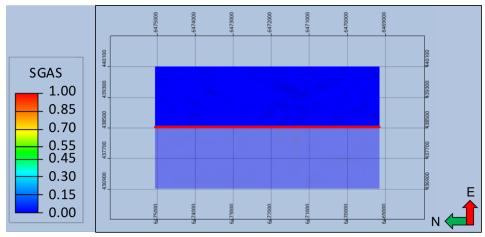

(a) Legend of gas saturation and orientation of cross section. Cross section marked by red line, and viewed from the East.

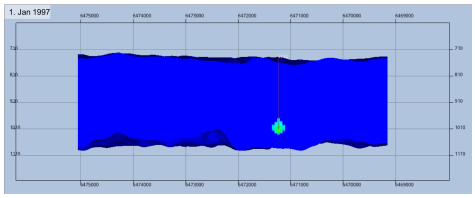

(b) Development 1. Jan 1997

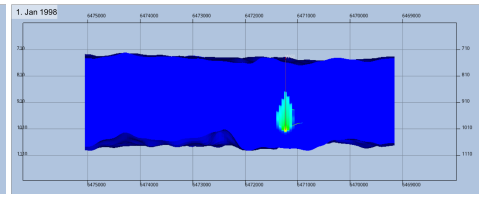

(c) Development 1. Jan 1998

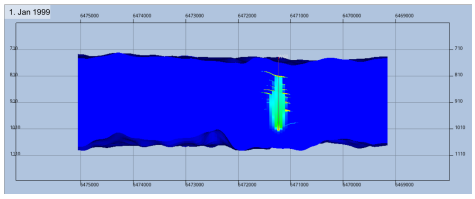

(d) Development 1. Jan 1999

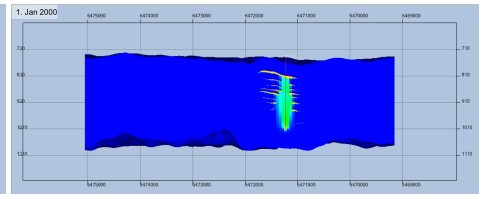

(e) Development 1. Jan 2000

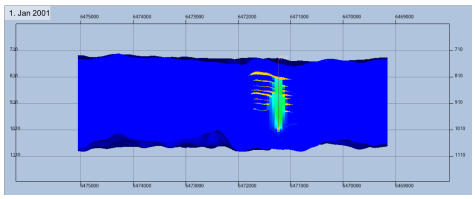

(f) Development 1. Jan 2001

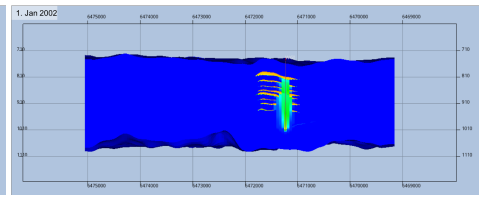

(g) Development 1. Jan 2002

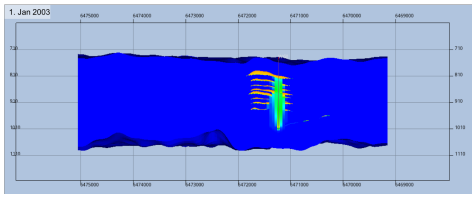

(h) Development 1. Jan 2003

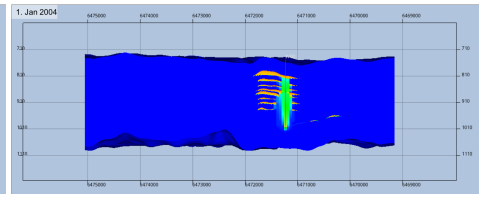

(i) Development 1. Jan 2004

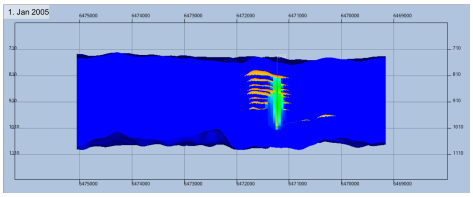

(j) Development 1. Jan 2005

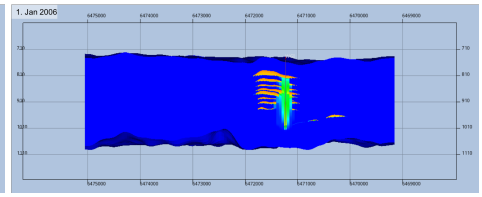

(k) Development 1. Jan 2006

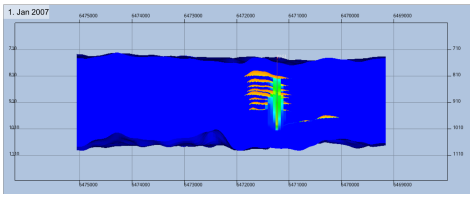

(l) Development 1. Jan 2007

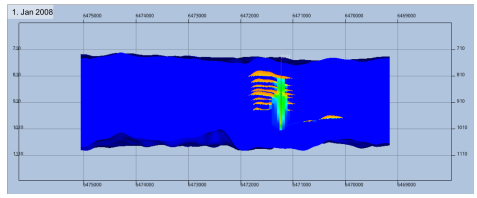

(m) Development 1. Jan 2008

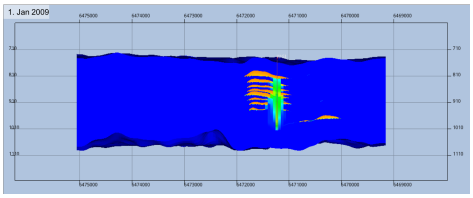

(n) Development 1. Jan 2009

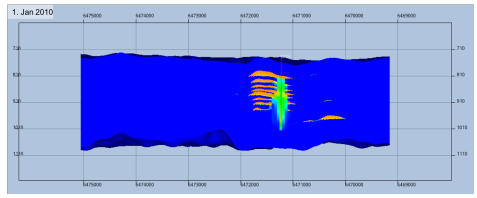

(o) Development 1. Jan 2010

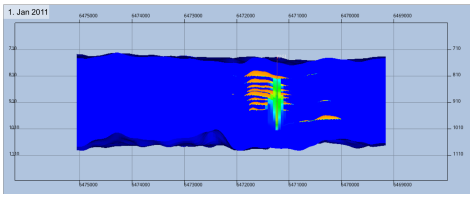

(p) Development 1. Jan 2011

Figure A.5: Plume development of the Case 2.4 with restricted permeability in the MFC simulation. Visualized in ResInsight. Model viewed from the East. Cells with gas saturation. Viewed with a range filter, the cells 32-64.

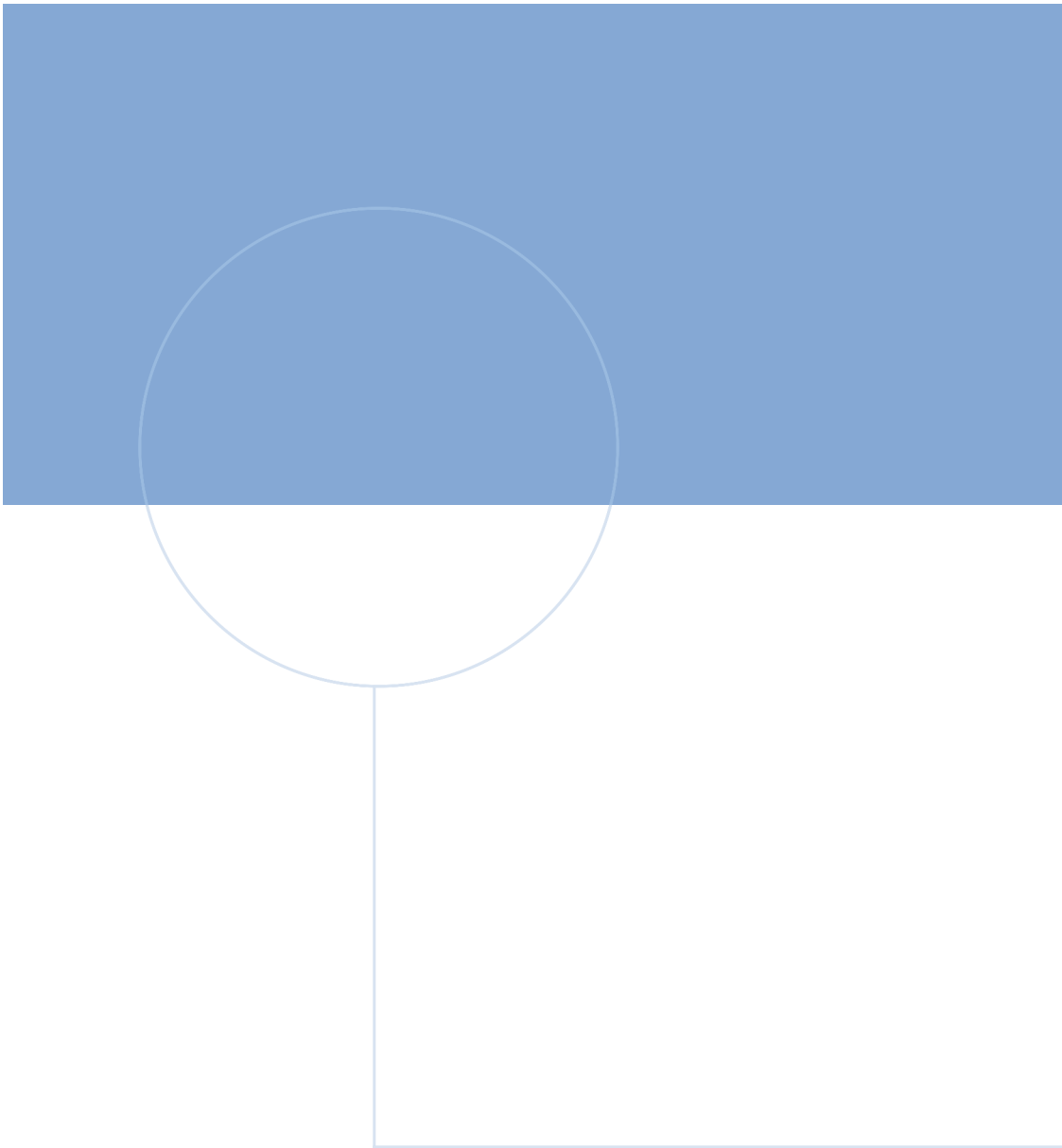

NTNU

Norwegian University of
Science and Technology